Monthly Notices
of the
ROYAL ASTRONOMICAL SOCIETY

MNRAS **471,** 4587–4605 (2017)
Advance Access publication 2017 July 21

doi:10.1093/mnras/stx1819

Simulations of the galaxy cluster CIZA J2242.8+5301 – I. Thermal model and shock properties

J. M. F. Donnert,[1,2]★ A. M. Beck,[3] K. Dolag[3] and H. J. A. Röttgering[4]

[1]*INAF Istituto di Radioastronomia, via P. Gobetti 101, I-40129 Bologna, Italy*
[2]*School of Physics and Astronomy, University of Minnesota, Minneapolis, MN 55455, USA*
[3]*University Observatory Munich, Scheinerstr. 1, D-81679 Munich, Germany*
[4]*Leiden Observatory, Leiden University, PO Box 9513, NL-2300 RA Leiden, the Netherlands*

Accepted 2017 July 17. Received 2017 July 14; in original form 2017 March 16

ABSTRACT

The giant radio relic in CIZA J2242.8+5301 provides clear evidence of an Mpc-sized shock in a massive merging galaxy cluster. Here, we present idealized SPH hydrodynamical and collisionless dark matter simulations, aiming to find a model that is consistent with that large range of observations of this galaxy cluster. We first show that in the northern shock, the observed radio spectral index profile and integrated radio spectrum are consistent with the observed upstream X-ray temperature. Using simulations, we first find that only a cool-core versus non-cool-core merger can lead to the observed elongated X-ray morphology. We then carry out simulations for two merging clusters assuming a range of NFW and β-model density profiles and hydrostatic equilibrium. We find a fiducial model that mimics the overall morphology of the shock structures, has a total mass of $1.6 \times 10^{15}\,\mathrm{M}_{\odot}$ and a mass ratio of 1.76. For this model, the derived Mach number for the northern shock is 4.5. This is almost a factor 2 higher compared to the observational determination of the Mach number using X-ray observations or measurements of the radio injection spectral index. We could not find numerical models that both fit the X-ray properties and yielded such low Mach numbers. We discuss various ways of understanding this difference and argue that deep X-ray observations of CIZA J2242.8+5301 will be able to test our model and reconcile the differences.

Key words: shock waves – galaxies: clusters: general – galaxies: clusters: intracluster medium.

1 INTRODUCTION

Merging galaxy clusters are among the most energetic events in the Universe. More than 10^{63} erg of potential energy is released and dissipated in the intercluster medium (ICM) on a time-scale of a Gyr (Sarazin 2002; Kravtsov & Borgani 2012). Most of this energy is directed into heat through compression and shocks. These processes can be observed using X-ray satellites, which find signatures of shocks and cold fronts in many clusters (Sarazin 1988; Markevitch & Vikhlinin 2007). A small part of the potential energy has been argued to stir turbulence, amplify magnetic fields and accelerate relativistic particles (Brunetti & Jones 2014). These processes result in giant radio relics in many shocks and giant radio haloes associated with the turbulent ICM of many merging clusters (Govoni & Feretti 2004; Brüggen et al. 2012; Feretti et al. 2012).

A cluster prominently hosting all of these features is CIZA J2242.8+5301, the 'Sausage cluster'. Discovered by van Weeren et al. (2010), its nickname was coined after the northern relic of the cluster, which is evidence for a unique large shock propagating in the ICM. CIZA J2242.8+5301 itself is among the most well-observed relic clusters in existence. Observational studies focus on the northern relic (Stroe et al. 2013, 2014b, 2016; Akamatsu et al. 2015), the mass distribution (Dawson et al. 2015; Jee et al. 2015; Okabe et al. 2015), the structure of the thermal ICM (Akamatsu & Kawahara 2013; Ogrean et al. 2013, 2014; Akamatsu et al. 2015) or the galaxy population (Stroe et al. 2014a, 2015; Sobral et al. 2015). Theoretical studies address the problem of radio spectral steepening in the relic (Stroe et al. 2014c; Kang & Ryu 2015; Basu et al. 2016; Kang & Ryu 2016) and magnetic field amplification in the shock (Iapichino & Brüggen 2012; Donnert et al. 2016). First simulations of the system have been presented early on by van Weeren et al. (2011).

Observations find different Mach numbers for the shocks and in the two relics. Mach numbers derived from the total integrated radio spectrum are in the range of $M = 4.6^{+1.3}_{-0.9}$ in the north and 2.8 ± 0.19 in the south (Stroe et al. 2013). Lower radio Mach numbers in the northern relic have been reported by Hoang et al. (2017), who find $M = 2.6$ from the largest spectral index between 150 MHz (LOFAR) and 610 MHz (GMRT). Stroe et al. (2014c) report $M = 2.8$

★ E-mail: donnert@ira.inaf.it

© 2017 The Authors
Published by Oxford University Press on behalf of the Royal Astronomical Society

Downloaded from https://academic.oup.com/mnras/article-abstract/471/4/4587/4002678 by guest on 20 November 2018

in the northern relic from spectral age modelling using the BRATS software package (Harwood et al. 2013). They note however that the CR electron cooling is inconsistent with this Mach number and implies a downwind speed of 1400 km s^{-1}. Their model implies a speed of 900 km s^{-1}. These estimates agree with the Mach number inferred from the X-ray-derived temperature jump across the shock: Akamatsu et al. (2015) find $M = 2.7^{+0.7}_{-0.5}$ and $M = 1.7^{+0.4}_{-0.3}$ in the two shocks, respectively. *Chandra* observations marginally detected the surface brightness jump at the northern relic and inferred $M = 1.3$ (Ogrean et al. 2014).

Differences in Mach number have significant implications for the shock energetics and thus models for cosmic ray injection and acceleration, and for magnetic field amplification, as the shock flux scales with the shock velocity to the third power. However, at this point it remains unclear, which Mach number scenario is correct in the 'Sausage' relic:

(i) Mach numbers inferred from the slope of the integrated spectrum can be model dependent and its steepening above 8 GHz not fully understood. The spectrum can suffer from instrumental effects due to differences in UV coverage of the radio telescopes involved (see Brunetti et al. 2013, for a discussion of instrumental effects on the Coma radio halo). This is especially true, if single dish and radio interferometers are combined (Stroe et al. 2016). However, for the northern relic in CIZA J2242.8+5301, the Mach number estimates are based on data at more than 10 frequencies, all from radio interferometers, carefully reduced from the raw data by the same observer with matched UV coverage (Stroe et al. 2016). The integrated spectrum does not suffer from projection or resolution effects as long as the extraction regions of the total flux are roughly consistent between frequencies and point source removal is not an issue.

(ii) In contrast, spectral index maps measure the slope locally and are less dependent on the underlying model. However, observations are potentially prone to resolution and projection effects. In the Sausage, Hoang et al. (2017) argue that at their high spatial resolution CRe cooling within the resolution of the observations (<10 kpc) does not play a role and projection effects are negligible in a spherical shock. However, the exact geometry of the shock remains unclear.

(iii) In the X-rays, Mach number estimates are independent of the involved non-thermal modelling required at radio frequencies. However, as the shock is at the outskirts of the cluster, count rates and thus statistics in the spectrum are notoriously low. Consequently, the shock surface of the northern shock (NS) has not been detected, so the surface brightness jump cannot be reliably used to estimate the Mach number (Ogrean et al. 2014 give a Mach number of 1.3, albeit very close to the background). The best Mach number estimates are based on the temperature jump inferred from *Suzaku* data. Here, the limited spatial resolution of the instrument mixes regions of different temperature, so an exact estimate right behind the shock is not possible. Furthermore, most instruments have very limited sensitivity at energies above 10 keV, which may introduce a bias towards low temperatures and thus lower Mach numbers.

In other clusters, Mach numbers inferred from the X-ray temperature jump and the integrated radio spectral index are sometimes consistent: e.g. Bullet cluster (Shimwell et al. 2015), El Gordo (Botteon et al. 2016), but inconsistent in the Toothbrush cluster (Kang, Ryu & Jones 2017). The cause of these differences is not known.

Cosmological simulations generally find an abundance of internal cluster shocks with Mach numbers of 2 and above (e.g. Miniati et al. 2000; Pfrommer et al. 2006; Hoeft et al. 2008; Skillman et al. 2008; Vazza, Brunetti & Gheller 2009; Hong et al. 2014; Schaal et al. 2016). Internal shocks with Mach numbers of more than 3 are found only in major mergers, so the high radio derived Mach number cannot be generally excluded on these grounds. Mach numbers of 5 and above appear only in cluster accretion shocks outside of the virial radius. Hong, Kang & Ryu (2015) show that the projection of multiple shocks can potentially lead to an inconsistency in radio and X-ray-derived Mach numbers in some cases. However, the size and homogeneity of the relic in the north of CIZA J2242.8+5301 make an overlap of several shocks seem unlikely.

In this paper, we aim to find a numerical model for CIZA J2242.8+5301 that is consistent with the observations of the system. Significant new observational constraints emerged since the last numerical study of the cluster was attempted by van Weeren et al. (2011). Furthermore, this study did not fully account for the DM dynamics of the system, which we model self-consistently. We can now also directly compare to the new weak lensing data. A consistent numerical picture of the system can provide clues to where to search for new observational evidence to reconcile the inconsistency in the Mach numbers in the shock and the relic.

We will use an idealized numerical model for merging galaxy clusters. Such models give us full control over the many merger parameters and allow us to efficiently explore the rather large parameter space (Burns et al. 1993; Schindler & Mueller 1993; Roettiger, Burns & Stone 1999; Lage & Farrar 2014; ZuHone & Kowalik 2016). CIZA J2242.8+5301 is ideally suited for these kinds of simulations, as in contrast to other systems like the Toothbrush cluster, it is likely a simple two-body merger.

This paper is structured as follows. We begin with a review and discussion of the current constraints for CIZA J2242.8+5301 from observations, and present our approach in Section 2. We outline our numerical model for spherically symmetric galaxy clusters and its implementation in Section 3. The results from the resulting simulations are elaborated in Section 5 and discussed in Section 6. We draw our conclusions at the end in Section 7. We use a concordance cosmology with $h_{100} = 0.7$, $\Omega_\Lambda = 0.7$ and $\Omega_M = 0.3$

2 MODELS FOR CIZA J2242.8+5301

2.1 Observational constraints

Currently, CIZA J2242.8+5301 is among the best observed galaxy clusters in all of astronomy, especially in the radio band. Placed at a redshift of $z = 0.188$ (Dawson et al. 2015), the weak lensing study by Jee et al. (2015) finds subcluster masses[1] of $M_{south} = 9.8^{+0.38}_{-0.25} \times 10^{15}$ $M_\odot$ and $M_{north} = 1.1^{+0.37}_{-0.32} \times 10^{15}$ $M_\odot$ with both mass peaks about $d_{peak} = 1 \pm 0.15$ Mpc apart. Another analysis of the same data by Okabe et al. (2015) yields $M_0 = 1.096^{+0.982}_{-0.567} \times 10^{15}$ $M_\odot$, $M_1 = 0.551^{+0.639}_{-0.343} \times 10^{15}$ $M_\odot$ and $d_{peak} = 712$ kpc, roughly consistent with the previous study. The probability distribution in the plane of subcluster masses from the former study are shown in Fig. 1 (see Section 2.2), we add the constraints of the latter study as dashed box. These masses carry significant systematic uncertainties of up to a factor of 2, because the mass distribution along the line of sight is not known and often assumed spherical, i.e. ignoring halo triaxiality (Corless & King 2007).

ROSAT finds a luminosity of $L_x = 6.4 \times 10^{44}$ erg s^{-1} at 0.2–2.4 keV (Kocevski et al. 2007). This brightness is roughly consistent with the value obtained by *Chandra* (5.65×10^{44} erg s^{-1},

[1] We give all masses relative to a top hat over density of $\Delta = 200$.

Downloaded from https://academic.oup.com/mnras/article-abstract/471/4/4587/4002678 by guest on 20 November 2018

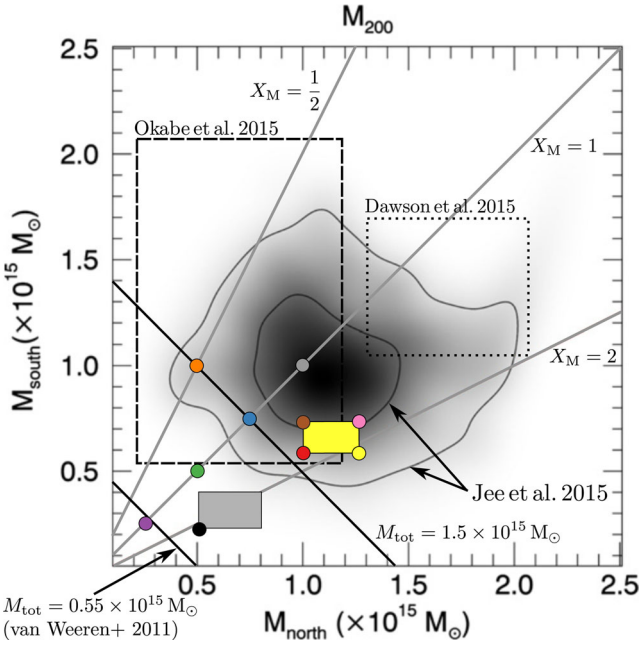

Figure 1. In contours, the 2σ and 1σ confidence intervals of cluster masses from the weak lensing study (adapted from Jee et al. 2015), weak lensing results from Okabe et al. (2015) as black dashed box, strong lensing results from Dawson et al. (2015) as black dotted box. Numerical models from this study as coloured dots. We mark the lines with $M_{\rm tot} = 0.55 \times 10^{15}$ M$_\odot$ (van Weeren et al. 2011) and $M_{\rm tot} = 1.5 \times 10^{15}$ M$_\odot$ as black lines. Lines with $X_{\rm M} = 0.5, 1, 2$ as grey lines. The region of fiducial models with $r_{\rm cut} = 1.7\, r_{200}$ is marked yellow, the plane with $r_{\rm cut} = 10\, r_{200}$ in grey. See Section 4 for details.

0.5–2.4 keV, Akamatsu & Gu, private communication). *Suzaku* observations by Akamatsu et al. (2015) find a temperature jump at the NS from $T_{\rm up,NS} = 2.7^{+0.9}_{-0.5}$ keV to $T_{\rm dw,NS} = 8.5^{+0.8}_{-0.6}$ keV, implying a Mach number of $M_{\rm NS} = 2.7$. At the southern shock (SS), $T_{\rm up,SS} = 5.1^{+1.5}_{-1.2}$ keV and $T_{\rm dw,SS} = 9^{+0.6}_{-0.6}$ keV, implying $M_{\rm SS} = 1.7$.

Radio observations find a radio halo and two radio relics at a distance of 2.8–3.2 Mpc, both exceeding 2 Mpc size at low frequencies (Stroe et al. 2016; van Weeren et al. 2010; Hoang et al. 2017). Comparing weak lensing and radio observations, we find that the northern relic has a distance of $d_{\rm NR} \approx 2$ Mpc from the southern core, and the SR $d_{\rm SR} \approx 2$ Mpc for the northern core, a remarkably symmetric configuration.

The northern relic (NR), the 'Sausage', is remarkably homogeneous and thin, with an average Mach number of $M_{\rm NR} \approx 4.6$, inferred from the integrated radio spectrum at 16 frequencies between 150 MHz and 3 GHz. However, Mach numbers derived from either the flattest observed radio spectral index in the relic or spectral age modelling are consistent with the X-ray-derived Mach number, with around $M = 2.6$ (Stroe et al. 2014c; Hoang et al. 2017). We note that Mach number estimates from the spectral index are potentially biased low due to mixing of CRe electron populations within the radio beam or due to projection effects. Hoang et al. (2017) argue that these effects are minimal in the Sausage, because no significant cooling takes place at 150 MHz within their spatial resolution of <10 kpc and the relic may have the form of a spherical cap.

The irregular southern relic (SR) has $M_{\rm SR} \approx 2.7$ (van Weeren et al. 2010; Stroe et al. 2016; Hoang et al. 2017). In the simplest models, the spectral index profile of the NR is well fitted by a downwind shock speed $v_{\rm dw,NR} \geq 1200\,{\rm km\,s^{-1}}$ (Stroe et al. 2014c; Donnert et al. 2016). This has also been inferred by spectral age models in Stroe et al. (2014c).

2.2 Approach

The observed X-ray morphology of the system is clearly elongated along the merger axis. A simulated merger of two disturbed clusters with similar mass at small impact parameter leads to a displacement of both ICMs so that the overall shape of the X-ray emission is not consistent with this narrow elongated shape observed in CIZA J2242.8+5301 by *Chandra*. We show and discuss a simulated of such a model in the Appendix. Hence, we adopt the working hypothesis that the northern progenitor was a cool-core cluster, which is breaking up during the ongoing merger with the southern progenitor This naturally motivates the regular shape of the NR: to maintain a regular shape over its traveltime of 0.5–1.0 Gyr, the shock must have propagated through a cone free of larger fluctuations in sound speed/temperature and density on scales of 2 Mpc. Such a homogeneous and quiet ICM, free of bulk flows, means that the progenitor cannot be subject to a major merger within 1–2 Gyr prior to the current merger, which makes a cool-core morphology very likely.

This is in contrast to the SR, which is rather irregular. Indeed, cosmological simulations suggest that this difference in shock structure is common in merging clusters (Schaal et al. 2016).

To find a model for CIZA J2242.8+5301 that is consistent with the majority of observations, we first consider the NS to constrain its upstream medium and thus the progenitor of the southern subcluster. We can relate X-ray and radio observations with our model and its mass predictions with global cluster properties like weak lensing masses and X-ray brightness.

2.2.1 *High Mach number scenario*

In the high Mach number scenario, we assume that the Mach number from the integrated radio spectrum and the downwind speed from the radio spectral index profile are correct. Thus, we adopt a canonical Mach number of $M = 4.6$. The Rankine–Hugoniot jump conditions then give a compression factor of $\sigma_{\rm NR} = 3.5$. The downstream shock velocity inferred from the radio spectral index profile is $v_{\rm dw,NR} \approx 1200\,{\rm km\,s^{-1}}$, this gives an upstream velocity of $v_{\rm up,NR} = 4200\,{\rm km\,s^{-1}}$. As

$$M = \frac{v_{\rm up}}{c_{\rm s}}, \tag{1}$$

this corresponds to a sound speed of $c_{\rm s,NR} = 918\,{\rm km\,s^{-1}}$ ahead of the shock or a temperature of $T \approx 3.6 \times 10^7$ K $= 3.1$ keV. This is roughly consistent with the X-ray measurements for the upstream temperature of $2.9^{+0.9}_{-0.5}$ keV. The same estimates can be made for the SS and progenitor. However, without velocity constraints from the SR, which is highly irregular and possibly contaminated by outflows from close-by galaxies, a spectral index profile does not lead to a clear downwind temperature. The upstream temperature from the X-rays (5 keV) gives $c_{\rm s,SR} \approx 1180\,{\rm km\,s^{-1}}$, which with the $M_{\rm SR} = 2.7$ gives $v_{\rm up,SR} = 3305\,{\rm km\,s^{-1}}$. We call this parameter set of Mach numbers, upstream temperatures and shock velocities the *high Mach number scenario*.

2.2.2 *Low Mach number scenario*

In this scenario, we assume that the Mach number inferred from the X-ray temperature jump and recent LOFAR/GMRT spectral

Downloaded from https://academic.oup.com/mnras/article-abstract/471/4/4587/4002678 by guest on 20 November 2018

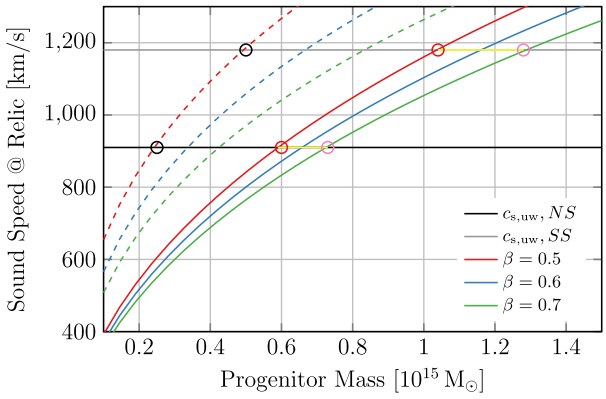

Figure 2. Sound speed at 2 Mpc versus progenitor mass for $\beta = 0.5$, 0.6, 0.7 in red, blue and green respectively. We include the upstream sound speed inferred from observations as black and grey horizontal lines. We plot the shock speed for $r_{\rm cut} \to \infty$ as dashed lines. The yellow lines mark the mass range of fiducial models for high Mach number scenario (see Section 3). We circle progenitor masses of the Black, Red and Pink models in their respective colours.

index maps is correct. To this end, we turn around above arguments to predict the shock velocity from the measured X-ray temperature jump. The X-ray-derived Mach number of $M_{\rm NS} = 2.7$ requires $v_{\rm up,NS} = 2300\,{\rm km\,s^{-1}}$ upstream of the NS. In the SS we infer from the X-ray temperatures: $v_{\rm up,SS} = 2040\,{\rm km\,s^{-1}}$. We call this parameter set, which is inconsistent with the radio parameter set, the *low Mach number scenario*.

The difference in shock speed in the two scenarios ($v_{\rm up,NR} \approx 2v_{\rm up,NS}$) illustrates the inconsistency of the X-ray and radio observations independently of cluster properties like temperature or mass.

2.2.3 *Mass range*

As the ICM ahead of the shock has not been affected by the merger, we can use the upstream sound speed to choose the total mass of the progenitor given its β-model and the distance to the progenitor mass peak. In Fig. 2, we plot the sound speed at $d_{\rm Relic} = 2\,{\rm Mpc}$ over progenitor mass for a model with β equal to 0.5, 0.6 and 0.7 in red, green and blue, respectively. We also overplot the observed upstream sound speed in the NR (SR) as black (grey) line. From the intersection of model sound speed with observed sound speed, we find that both are consistent in a mass range from $M_0 = 0.59$–0.73×10^{15} M$_\odot$ (yellow line), depending on the value of β. This mass range is also roughly consistent with the weak lensing value of the southern subcluster $M_{\rm south} = 0.98^{+0.38}_{-0.25} \times 10^{15}$ M$_\odot$ (yellow area in Fig. 1).

For the SR at a distance of 2 Mpc, our model predicts a mass of $M_1 = 1.04$–1.28×10^{15} M$_\odot$ (Fig. 2). This is again consistent with the weak lensing estimate for the northern subcluster of $M_{\rm north} = 1.1 \pm 0.3 \times 10^{15}$ M$_\odot$. We will attempt to use our simulations to predict the kinematics of mergers from these models, the expected shock morphology and velocity and the location of the DM mass peaks.

3 CLUSTER MODEL

We follow an approach similar to Donnert (2014, D14 hereafter) to set up initial conditions for collisionless DM particles and smoothed particle hydrodynamics (SPH) particles. We define the mass of the cluster as M_{200} and then find r_{200} as the radius where the average density of the cluster is Δ times the critical density at cluster redshift z with $\Delta = 200$. We assume the canonical baryon fraction ($b_{\rm f}$) of 17 per cent in r_{200} to find DM mass and ICM mass. A cluster is then completely defined by its DM and ICM density profiles and the assumption of hydrostatic equilibrium. We use an NFW profile for the DM density and a beta-model for the ICM density (Cavaliere & Fusco-Femiano 1976; Navarro, Frenk & White 1996). Convergence demands that the models are cut-off at large radius: the NFW profile at the sampling radius $r_{\rm sample}$, which we set to half the box size or $1.2r_{200}$. The exact value is not important as the collisionless particle mix within 20 Myr into a smooth distribution. We only make sure that the distribution within r_{200} is unaffected. We cut-off the gas density (β-model) at $r_{\rm cut}$:

$$\rho_{\rm DM} = \frac{\rho_{0,\rm DM}}{\frac{r}{r_{\rm s}}(1+\frac{r}{r_{\rm s}})^2}\left(1+\frac{r^3}{r^3_{\rm sample}}\right)^{-1} \tag{2}$$

$$\rho_{\rm gas} = \rho_{0,\rm ICM}\left(1+\frac{r^2}{r^2_{\rm core}}\right)^{-\frac{3}{2}\beta}\left(1+\frac{r^3}{r^3_{\rm cut}}\right)^{-1}. \tag{3}$$

We then find the cumulative mass profiles, temperature profile and relative gravitational potential ($\Psi = -\phi$) profiles from numerical integration using Gaussian quadrature from the GSL library (GSL Project 2010):

$$M(<r) = 4\pi\int_0^r \rho(t)\,t^2{\rm d}t \tag{4}$$

$$T(r) = \frac{\mu m_{\rm p}}{k_{\rm B}}\frac{G}{\rho_{\rm gas}(r)}\int_r^{R_{\rm max}}\frac{\rho_{\rm gas}(t)}{t^2}M_{\rm tot}(<t)\,{\rm d}t \tag{5}$$

$$\Psi(r) = G\int_0^r \frac{M(<t)}{t^2}\,{\rm d}t, \tag{6}$$

where G is Newton's constant, $k_{\rm B}$ is Boltzmann's constant, $m_{\rm p}$ is the proton mass and $\mu \approx 0.6$ is the mean molecular mass of the ICM plasma. We find the NFW scale radius $r_{\rm s}$ from the concentration parameter (Duffy et al. 2008) and set the core radius $r_{\rm core} = r_{\rm s}/3$ for the non-cool-core and $r_{\rm core} = r_{\rm s}/9$ for the cool-core models, see D14 and references therein.

To set the DM particle velocities we use rejection sampling (Press et al. 1992) from the particle distribution function $f(E)$. It is found from the combined gravitational potential of the gas and DM by numerically solving Eddington's equation (Eddington 1916; Kazantzidis, Magorrian & Moore 2004; Binney & Tremaine 2008; Barnes 2012):

$$f(E) = \frac{1}{\sqrt{8}\pi^2}\int_0^E \frac{{\rm d}\Psi}{\sqrt{E-\psi}}\frac{{\rm d}^2\rho}{{\rm d}\Psi^2} \tag{7}$$

by interpolating $\rho(\Psi)$ with a cubic spline and obtaining its second derivative directly from the spline.

We require an accurate SPH representation of the gas density distribution in our cluster model. Poisson sampling the ICM density field results in unacceptably large SPH sampling errors of >20 per cent, severely affecting the hydrostatic equilibrium of the system. We use the technique of weighted Voronoi tessellations to regularize the particle distribution and obtain smooth SPH densities (Diehl et al. 2012). We define a global density model as the maximum of the gas density of all clusters at a given position. A displacement can then be found from a neighbour search/SPH loop, which we implement using a Peano–Hilbert sorted oct-tree

Downloaded from https://academic.oup.com/mnras/article-abstract/471/4/4587/4002678 by guest on 20 November 2018

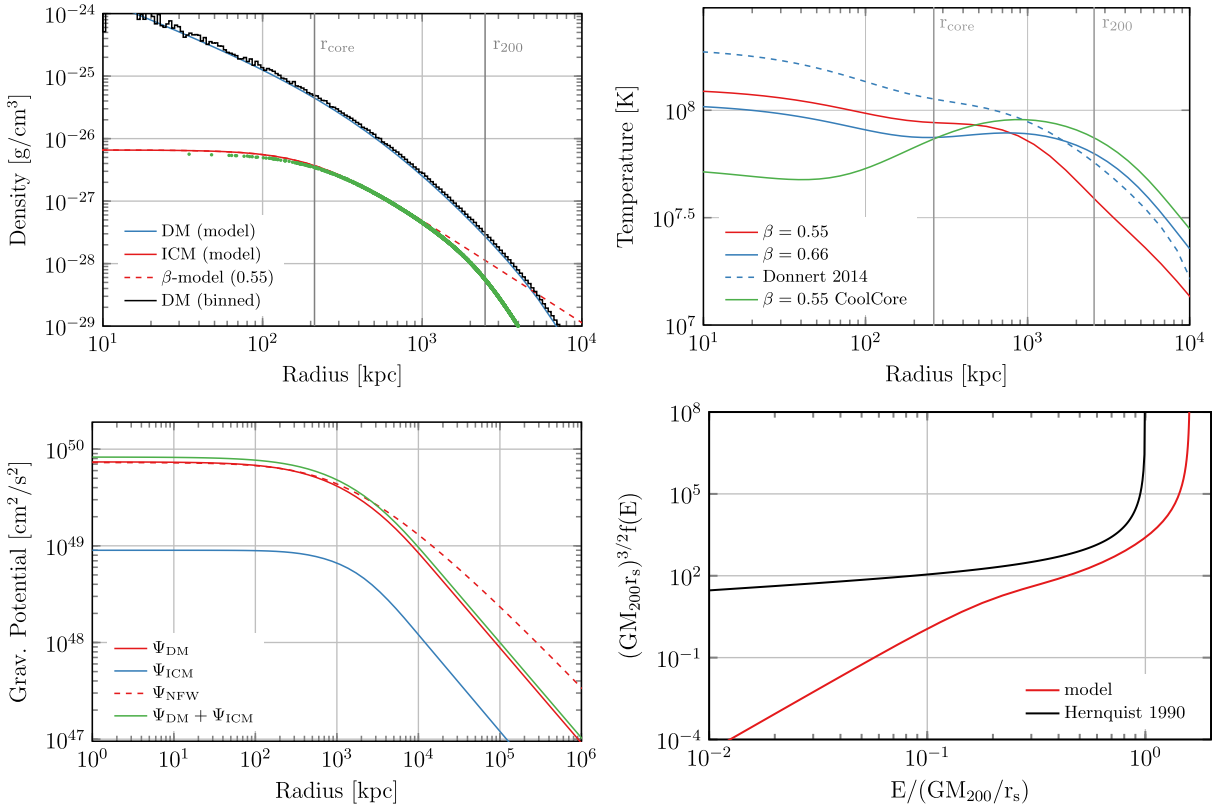

Figure 3. Initial conditions for a cluster with $M_{200} = 10^{15}$ M$_\odot$ (top left to bottom right): density profiles of gas (red), DM (blue), the standard β-model (red dashed), binned DM particles (black) and SPH density from a few thousand randomly selected WVT-regularized SPH particles (green dots); Top right: temperature profiles for values of $\beta = 0.66$ (blue) and 0.55 (red), a cool core with $\beta = 0.55$ (green) and the model from D14 (blue dashed); Bottom left: relative gravitational as generated from the DM density (red), the ICM (green), an NFW profile with the same DM mass (red dashed) and the sum of DM and ICM (green); Bottom right: distribution function of the DM particles (red) and from a Hernquist halo with the same mass (black). In the first two plots we mark r_{200} and r_{core} with vertical grey lines.

(e.g. Springel 2005). The algorithm regularizes the particle distribution in less than 20 iterations and the average SPH sampling error in density is reduced to less than 5 per cent. Test simulation shows that the resulting cluster models are numerically stable over several Gyr.

We implemented our refined model into the C code mentioned in D14. The techniques employed in the IC generation are scalable enough to easily allow the generation of models with hundred million particles on modern SMP machines. In Fig. 3, we show the model of a cluster with $M = 10^{15}$ M$_\odot$: in the first panel, we show the model density in red (ICM) and blue (DM) alongside the binned DM density (black line) and the SPH density on a random sample of 5000 SPH particles in green. We add the standard β-model as red dashed line, to show the effect of the cut-off in the ICM density. In the top right panel, we show the ICM temperature of the model and for a cluster with $\beta = 2/3$ as in D14. In these two panels, we mark the core radius and r_{200} as vertical grey lines. In the bottom left we show the relative gravitational potential (green) from the ICM (blue) and the DM (red). We add the potential from an NFW profile without cut-off as red dashed line. In the bottom right, we plot distribution function over relative energy $E = \Psi - v^2/2$ from the numerical solution of Eddington's formula (equation 7) using the combined DM and gas generated potential, alongside the standard Hernquist solution (black; Hernquist 1990).

3.1 Setting the cut-off radius

The cut-off radius r_{cut} has significant influence on the temperature structure of a cluster around its virial radius. To establish a fiducial value for the parameter in the mass range of interest, we determine the density and temperature profiles of the Perseus cluster with our model.

In Fig. 4, we show the influence of r_{cut} (equation 3) on density and temperature profiles fit to observations of the Perseus cluster. We show the de-projected profiles inferred from X-ray observations as black dots with error bars (Simionescu et al. 2011; Zhuravleva et al. 2013; Urban et al. 2014). In-line with previous fits, we find $M_{200} = 0.665 \times 10^{15}$ M$_\odot$, $r_{200} = 1810$ Mpc, $c_{NFW} = 7.7$, $r_{core} = 26$ kpc, $\beta = 0.56$. We plot the temperature for $r_{cut} = r_{200}$ (lighter red) and $r_{cut} = 1.7r_{200}$ (bright red) and $r_{cut} = 3r_{200}$ (dark red). We show $r_{cut} \to \infty$ as dotted line. We find that the cut-off radius has significant impact on the temperature profile around the virial radius, with a best fit of $r_{cut} \approx 1.7r_{200}$. We note that there is significant scatter in the data from the Perseus cluster. Depending on direction/arm of the observation, the data are consistent with $r_{cut} = r_{200}$ and $r_{cut} = 3r_{200}$ (Urban et al. 2014). Thus, r_{cut} is generally poorly constrained. None the less, a model without cut-off (dotted line) is inconsistent with the Perseus temperature data beyond 500 kpc, and thus not motivated.

Downloaded from https://academic.oup.com/mnras/article-abstract/471/4/4587/4002678 by guest on 20 November 2018

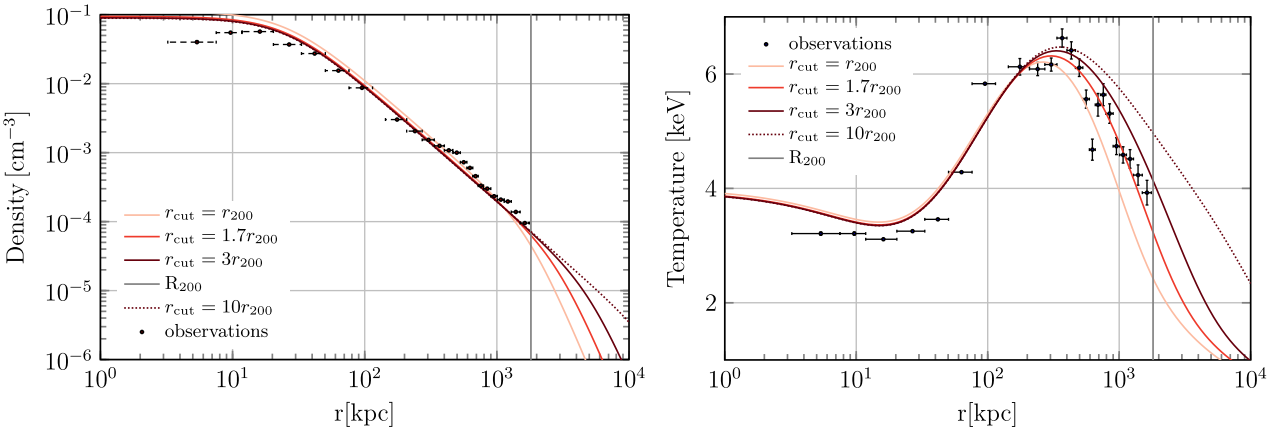

Figure 4. Left: density profiles of three models for the Perseus cluster with $r_{cut} = 1, 1.7, 3 \times r_{200}$ in light, bright and dark red, $r_{cut} \to \infty$ as dotted line. R_{200} as grey vertical line. Right: the same, but temperature profiles in keV. Observed profiles as black dots with error bars from Urban et al. (2014) and Zhuravleva et al. (2013).

4 NUMERICAL MODELS

Following D14, we model the northern progenitor as a cool-core cluster by setting $r_{core} = r_s/9$. The southern progenitor is modelled as disturbed motivated from the SR morphology with $r_{core} = r_s/3$. β is generally degenerate with cluster mass, Baryon fraction and has a strong influence on X-ray brightness. Thus, above considerations mark a region of acceptable progenitor masses in Fig. 1, which we mark yellow. Throughout this paper, we name models after their colour in this Fig. 1. Models Red, Pink, Yellow and Brown sample the corners of this region. The difference between NS and SS Mach number already suggest that the mass ratio is not exactly 1, regardless of the scenario.

We also consider models with $r_{cut} \gg r_{200}$, to check the influence of this parameter. This allows us to predict the lowest progenitor masses corresponding to the lowest potential energies and thus shock speeds possible in our approach. We overplot the sound speed at relic distance for a model with $r_{cut} \to \infty$ in Fig. 2 as dotted lines. Their intersection with the observed upstream temperatures gives mass of $M_0 = 0.25$–0.45×10^{15} M$_\odot$ for the northern progenitor and $M_1 = 0.5$–0.81×10^{15} M$_\odot$ for the southern progenitor (grey area in Fig. 1). We call the most conservative model allowed in this range the Black model.

Furthermore, we sample the plane of progenitor masses at mass ratios of 1 (see Fig. 1), adopting a universal value of $\beta = 0.6$ (models Grey, Blue, Green, Purple). We add another model with inverted mass ratio (Orange).

We parametrize the in-fall velocity as a fraction of the zero energy/Kepler orbit X_E, i.e. the velocity the clusters had if they were at rest at infinite distance (see also equation 8). $X_E = 1$ is the physical upper limit to the kinetic energy of the system. The lower limit is $X_E = 0$, i.e. progenitors are at rest when their distance is the sum of their virial radii r_{200}.

We focus on the total X-ray luminosity and shock speeds as well as Mach numbers of the simulations as predicted when the shocks are 3 Mpc apart. These fully determine the upstream and downstream temperatures of the shocks. We also aim to reproduce the elongated morphology of the X-ray emission. We first run all models with $X_E = 0$, which minimizes Mach number in the shocks and gives a rough estimate on the X-ray luminosity of the system at the observed state. We then increase the in-fall kinetic energy to $X_E = 0.5$.

We place the clusters at a distance so their virial radii touch and we set a small impact parameter of 50 kpc to break the otherwise near perfect symmetry of the system (CIZA J2242.8+5301 is likely a head on collision). An overview of all models is provided in Table 1.

We evolve all models with 10 million DM and 10 million SPH particles for 8 Gyr on the Itasca cluster of the Minnesota Supercomputing Institute at the University of Minnesota, using the latest version of the GADGET-3 code, including magnetic fields and shock finding (Springel 2005; Dolag & Stasyszyn 2009; Beck et al. 2016a; Beck, Dolag & Donnert 2016b). We use Smac2 (Donnert & Brunetti 2014) to compute projections from the simulation. X-ray brightnesses are given in the *ROSAT* band of 0.2–2.4 keV following Bartelmann & Steinmetz (1996). We project the spectroscopic temperature, which better approximates the observed X-ray temperatures than the simulated temperature (Mazzotta et al. 2004).

5 RESULTS

We identify the simulated with the observed system when the shocks have a distance of 3 Mpc. We find shock speeds and Mach numbers from the shock finder, where we use the mean of all particles with a Mach number above the 90th percentile of the distribution (Beck et al. 2016b).

5.1 Models with $X_M = 1$

We begin with results from models with $X_M = M_1/M_0 = 1$ and $X_E = 0$. They represent the most conservative lower limit on the kinetic energy in the system. It is not likely that two clusters form at the distance of their virial radii. Thus, we do not expect to find a well-fitting model with these simulations. Furthermore, a mass ratio of 1 minimizes the kinetic energy in the NS, because it matches the SS.[2] The goal is thus to obtain a lower limit on the shock velocities and the X-ray brightness in the merger state for different masses. We give basic model parameters, X-ray luminosities, Mach numbers and v_{travel} at the observed state in Table 1.

[2] This can easily be seen by considering a very large mass ratio. The smaller cluster will then not cause a large disturbance in the larger cluster.

Downloaded from https://academic.oup.com/mnras/article-abstract/471/4/4587/4002678 by guest on 20 November 2018

Table 1. Numerical models without initial velocity: mass (M_{200}) of progenitors, total mass, mass ratio, β parameter, X-ray luminosity at observed state, upwind shock speeds and time between core passage and observed state. Names correspond to the coloured dots in Fig. 1. Masses are in 10^{15} $M_\odot$, L_x is in 10^{44} erg s^{-1} in the *ROSAT* band of 0.2–2.4 keV, shock speeds from upper 75th percentile of the Mach number distribution in km s^{-1}, time in Myr.

Name/Colour	M_0	M_1	$M_{\rm tot}$	$X_{\rm M}$	β_0, β_1	$L_{\rm x}$	$M_{\rm NS}$	$M_{\rm SS}$	$v_{\rm NS}$	$v_{\rm SS}$	$t_{\rm travel}$
Grey	1	1	2	1	0.6, 0.6	14	3.9	4.5	4012	3897	600
Blue	0.75	0.75	1.5	1	0.6, 0.6	10	3.2	4.4	3215	3475	675
Green	0.5	0.5	1	1	0.6, 0.6	7.1	3.8	4.7	2833	2779	775
Purple	0.25	0.25	0.5	1	0.6, 0.6	3.7	3.7	5.0	1973	1972	1000
Red	0.59	1.04	1.63	1.76	0.5, 0.5	7	2.4	3.2	2996	2971	675
Yellow	0.59	1.28	1.88	2.13	0.5, 0.7	11	3.6	3.5	3748	3408	650
Brown	0.73	1.04	1.77	1.43	0.7, 0.5	15	2.5	3.2	3323	2887	650
Pink	0.73	1.28	2.01	1.75	0.7, 0.7	15	3.8	3.4	3771	3137	675
Orange	0.58	1.16	1.0	0.5	0.6, 0.6	9.6	3.2	2.2	2076	1794	975
Black	0.2	0.4	0.7	2.5	0.5, 0.5	1.8	3.0	3.1	2150	1837	700

In Fig. 5, panels 1–4, we show the projected X-ray luminosity of the four models. We find that the simulated X-ray emission has a triangular shape, less elongated than observed. The cool core has not broken up. Models with a total mass of $M_{\rm tot} = 1$–1.5×10^{15} $M_\odot$ are closest to the observed X-ray brightness. We also show the projected DM mass distribution in units of 10^{-21} g cm^{-2} as contours in Fig. 5. The distance between the DM mass peaks decreases with decreasing cluster mass. In all models but the heaviest one (Grey), the DM core has turned around, dragging ICM material with it. For the lowest mass model (Purple), the two mass peaks have a separation of less than a few hundred kpc. This is not compatible with the weak lensing observations that find a separation of about 1 Mpc with uncertainties of roughly 50arcsec $\approx$ 150 kpc per core (Jee et al. 2015; Okabe et al. 2015).

In Fig. 6, panels 1–4, we show the projected spectroscopic temperature of the models. All models show characteristic contact discontinuities, where the two ICMs pervade each other. This is likely a result of the idealized set-up and not realistic. In the real system, at least the southern progenitor has a disturbed morphology with bulk flows and density fluctuations that drive instabilities on multiple scales and facilitate mixing during the merger. This alters the X-ray morphology and temperature structure considerably (see Section 5.5). Temperatures in the shocks are in the range of 10–15 keV in the cluster centre of the larger systems, which is in-line with the observations.

All models show two symmetric shocks, whose size increases with decreasing cluster mass. We find temperatures in all shocks ranging from 15 to 25 keV, with the highest temperatures in the NS of the lowest mass model (Purple). Shock speeds range from 2000 to 4000 km s^{-1}, increasing with cluster mass and similar in the NS and SS. Mach numbers range from 3 to 5, with smaller Mach numbers in the NS. We speculate that the cool core drives the shock more efficiently than the disturbed progenitor.

In Fig. 7, we plot the Mach number from our shock finder in the NS (top) and SS (bottom) for the four simulations, adding the observed Mach numbers from the shock and relic as the dotted and the dashed line, respectively. In the NS, we find Mach numbers below 4, smaller than observed in the NR, and relative constant with cluster mass. In the SS, the simulated Mach numbers of 4.5–5 exceed observed ones significantly. This is in-line with our expectations from Section 2.2, where we argue for mass ratios above 1, resulting in larger M_1 and thus higher temperatures and lower shock speed ahead of the SS. Thus, models with $X_{\rm M} \leq 1$ are disfavoured by X-ray and radio data alike. Our exploratory simulations suggest that the observed system has a mass ratio above 1, a total mass of 1–1.5×10^{15} $M_{\rm sol}$ and $X_{\rm E} > 0$.

5.2 Models with $X_{\rm M} > 1$

We now consider models with mass ratios above 1 (Red, Pink, Yellow, Brown), also shown in Table 1. As shown above, every mass ratio implies a different values for the slope of the ICM profile (β). We find a strong dependence of the X-ray luminosity on this parameter. Only the Red model with $\beta_0 = \beta_1 = 0.5$ is close to the observed one, the other steeper models (Red, Pink, Yellow) are too bright (assuming a baryon fraction of 17 per cent). As shown in Fig. 5, panels 5–8, the shape of the X-ray emission remains triangular, with subtle differences among models. In all but the Yellow model the DM core of the northern progenitor has turned around. DM core separation is roughly 1 Mpc in all models. Temperature maps (Fig. 6, panels 5–8) show similar temperatures in the centre of the cluster as before.

Again two shocks are clearly visible in the temperature maps, with post-shock temperatures easily reaching 25 keV in the NS. However, only the SS is fully developed. Mach numbers of these shocks range from 2.4 to 3.9 in the NS and 3.2 to 3.5 in the SS (Table 1) with shock velocities around 3000 km s^{-1}. The Mach number distribution is shown in Fig. 8, with quite similar distributions in the SS. However, in the NS the Brown and the Yellow model show a tail in the distributions up to large Mach numbers of 4 and 5, respectively. This suggests that these two shocks are about to enter a region with lower temperatures and sound speeds, which boosts the Mach numbers significantly.

We conclude that the models are inconsistent with the high and the low Mach number scenario.

5.3 Models with initial velocity

We re-simulate models with mass ratios above 1 (Red, Yellow, Brown, Pink) with initial velocity, given by a zero energy orbit of $X_{\rm E} = 0.5$. This is a more realistic choice for the initial velocity, see Section 6.3 for a discussion. The initial velocity of the system is shown alongside X-ray brightness, Mach numbers and shock velocities in Table 2. We show projections of X-ray brightness and overlay them with DM density contours in Fig. 9, panels 1–4, and Mach number distributions in Fig. 11.

The total X-ray luminosity remains roughly unchanged with respect to the slow versions of the models, with the Red model

Downloaded from https://academic.oup.com/mnras/article-abstract/471/4/4587/4002678 by guest on 20 November 2018

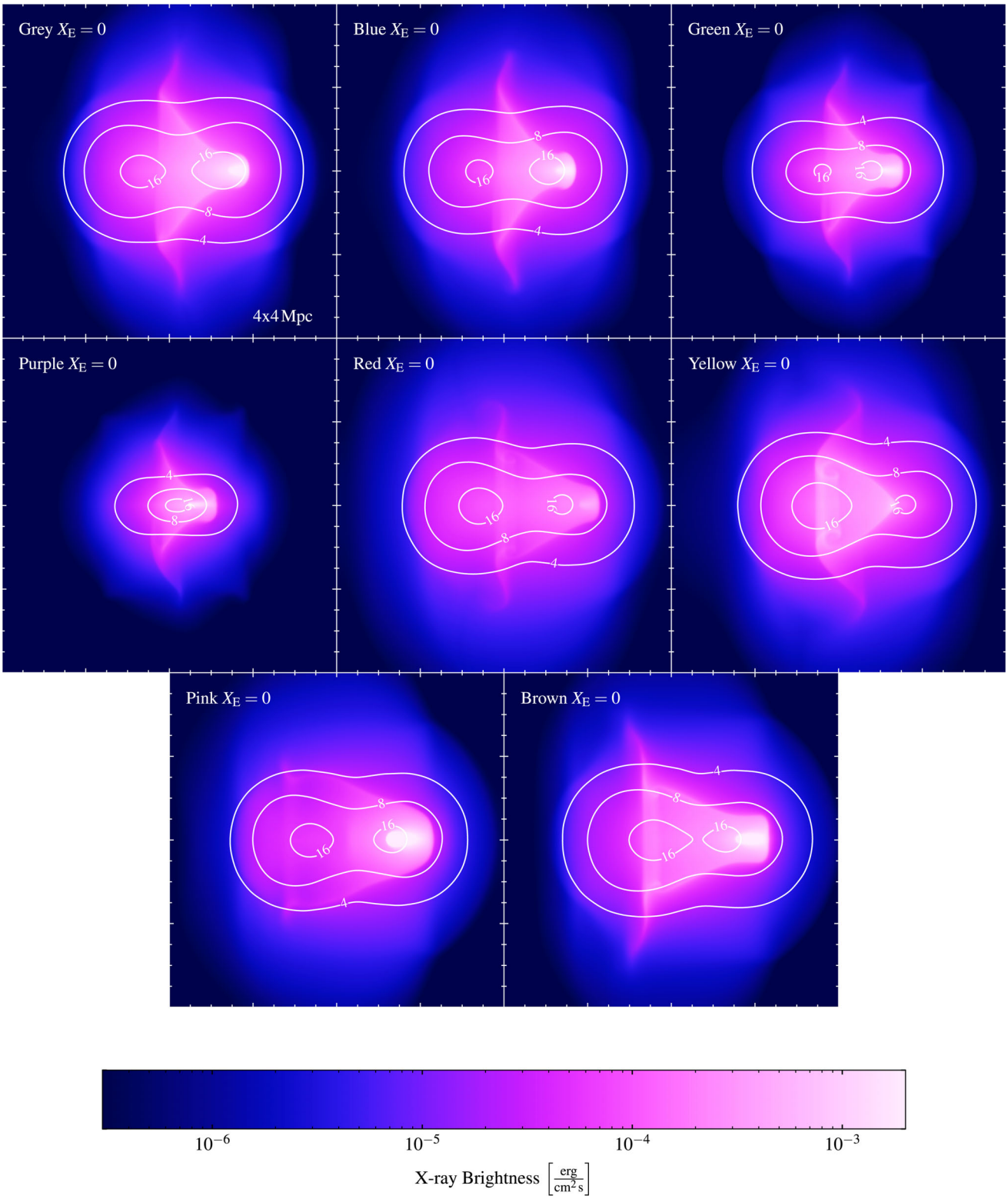

Figure 5. Projected X-ray emissivity of eight models with $X_E = 0$ (Grey, Blue, Green, Purple, Red, Yellow, Pink, Brown). We overplot contours of the DM mass distribution in 10^{21} g cm^{-2}.

reproducing the observed X-ray luminosity. The shape of the X-rays is now elongated along the merger axis, with models showing a mass peak separation of 1.2–0.7 Mpc, consistent with observations. Temperatures in the cluster centre are lower than in the slow models, around 10 keV consistent with observations.

Temperature projections in Fig. 10, panels 1–4, show two clear shocks in all models, with the NS significantly smaller than the SS. Temperatures in the NS reach 25 keV in all models, while it varies in the SS from 20 keV (Red, Pink) to above 25 keV (Yellow). Mach numbers in the NS are above 4.5, and low

Downloaded from https://academic.oup.com/mnras/article-abstract/471/4/4587/4002678 by guest on 20 November 2018

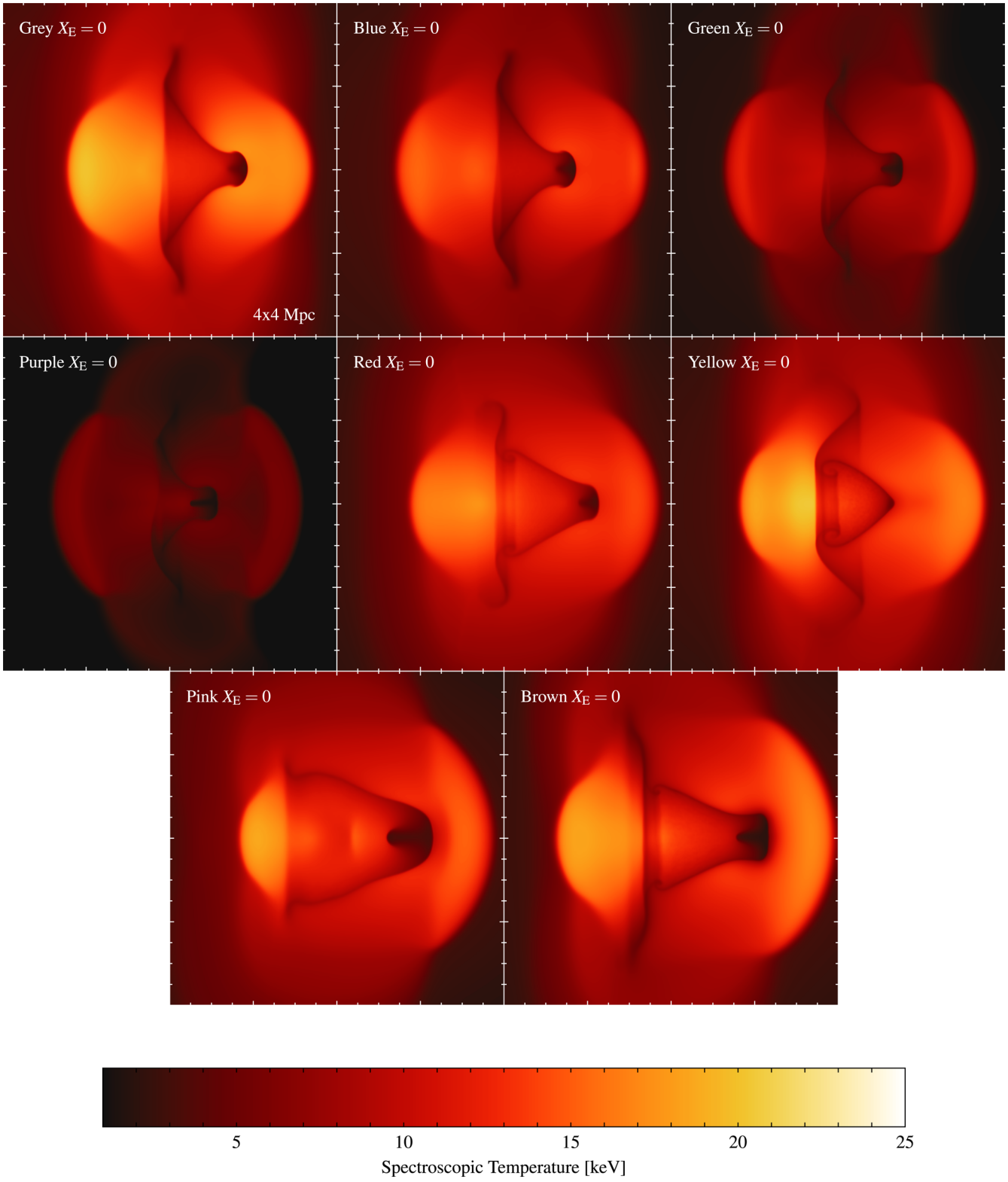

Figure 6. Projected Spectroscopic temperature of eight models with $X_E = 0$ (Grey, Blue, Green, Purple, Red, Yellow, Pink, Brown).

with around 3.5 in the SS. Shock velocities range from 4300 to 5300 km s^{-1} in the NS and 3300 to 4000 km s^{-1} in the SS. Mach number distributions (Fig. 11) confirm these values, with sharply peaked distribution at Mach numbers above 4.5 (NS) and 3.3 (SS). We conclude that the Red model is roughly consistent in the high Mach number scenario in Mach number and shock speed. However, the elongated size of the NS is too small by a factor of 2.

Downloaded from https://academic.oup.com/mnras/article-abstract/471/4/4587/4002678 by guest on 20 November 2018

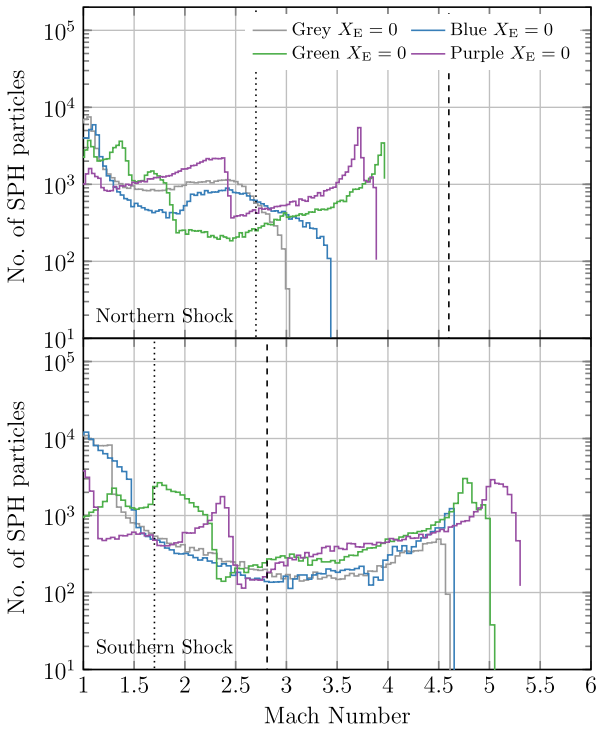

Figure 7. Binned Mach number distribution in the NS (top) and SS (bottom) from our Mach finder for models with $X_E = 0$ and $X_M = 1$. We also add the Mach number inferred from the radio (X-rays) in dashed (dotted) vertical line.

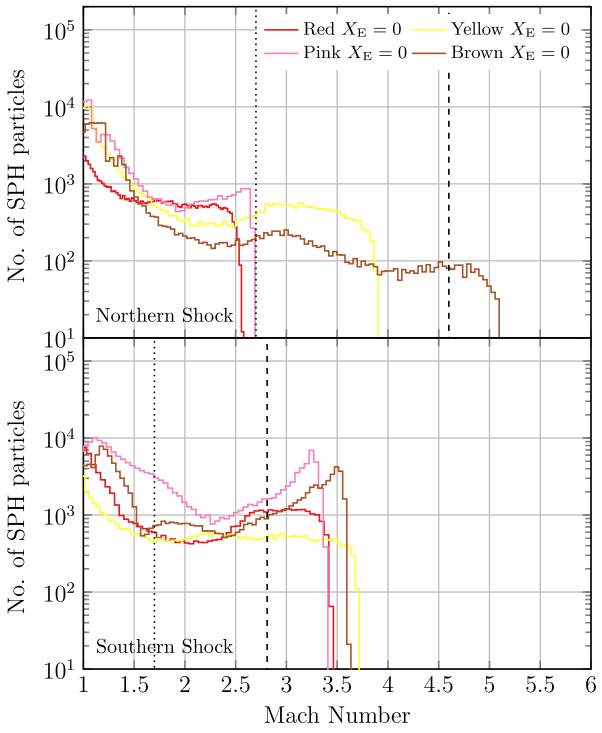

Figure 8. Binned Mach number distribution in the NS (solid) and SS (dashed) from our Mach finder for models with $X_E = 0$ and $X_M = 1$.

5.4 Two models with different baryon fractions

Here, we study the influence of the relative baryon fractions of the two progenitors on the system. We re-simulate the Red model, but reduce the baryon fraction of one progenitor from 17 per cent to 10 per cent. The other progenitor remains unchanged.

We show X-ray and temperature projections of the model where the southern progenitor has reduced baryon fraction ($b_{f,1} = 0.1$) on the left, the other one ($b_{f,0} = 0.1$) in Figs 9 and 10, panels 5 and 6. In the first case, we find that the SS is less prominent and a few hundred kpc smaller compared to the Red model. The NS is few hundred kpc larger than in the standard model. The X-ray morphology shows widening of the contact-discontinuities with respect to the standard model. The model with reduced b_f in the northern progenitor shows the opposite behaviour: The NS is suppressed to only 200 kpc, the SS hotter, but not much larger than before. The X-ray morphology is more narrow than before.

The Mach number distributions (Fig. 12) show nearly no change in Mach number for the first case (dashed red) when compared to the standard Red model. For the second case, the suppression of the NS reduces the Mach number with only a few 100 particles reaching 4 or above. The SS show lower Mach numbers here, likely because the southern progenitor cannot drive the shock as efficiently anymore.

We conclude that the shock morphology in the observed system points towards the first case, where the southern progenitor has a baryon fraction smaller than the northern progenitor ($b_{f,0} > b_{f,1}$).

5.5 Models with substructure

We re-simulate the Red model with standard baryon fraction $b_{f,0} = b_{f,1} = 0.17$ (red, solid) and reduced Baryon fraction in the southern progenitor $b_{f,0} = 0.17$, $b_{f,1} = 0.10$ (red, dashed). We include a population of subhaloes in the southern progenitor in both models. Subhalo mass distribution and spatial distribution depending on host mass are drawn from models for DM cluster substructure (Gao et al. 2004; Giocoli et al. 2010). The subhalo mass fraction is 0.23. To properly resolve the subhaloes, we introduce a lower mass limit so each halo contains at least 6000 particles (twice 10 times the number of kernel neighbours). The haloes are sampled up to the tidal radius (Tormen, Diaferio & Syer 1998) and are set on random orbits with the velocity limited to half the local sound speed at distances no larger than the virial radius from the centre of the host cluster. This way we add around 60 subhaloes with a mass range of a few 10^{12} $M_\odot$ to a few 10^{10} $M_\odot$. This allows us to investigate the influence on bulk motions and inhomogeneities in the flow on the merger state and the X-ray morphology. Of course the exact dynamics in the cluster centre as well as the pre-merger state cannot claim to be a realistic model for the cluster dynamics, because they are dominated by our artificial choice of the subhalo population. In our toy model this approach is merely a proof of concept.

In the beginning of the simulation, the subhaloes of the southern progenitor fall into the cluster centre, seeding instabilities and bulk flows by gas stripping, as expected. During core passage the main DM haloes interact and drive two shocks into the progenitor ICM. Shortly after the core passage most of the subhaloes are stripped of their gas. In the first 20 Myr after core passage, the cool core of the northern progenitor gets ablated by the additional bulk flows in the southern progenitor. Both shocks propagate into undisturbed medium, as the outer part of the southern progenitor remains undisturbed.

Downloaded from https://academic.oup.com/mnras/article-abstract/471/4/4587/4002678 by guest on 20 November 2018

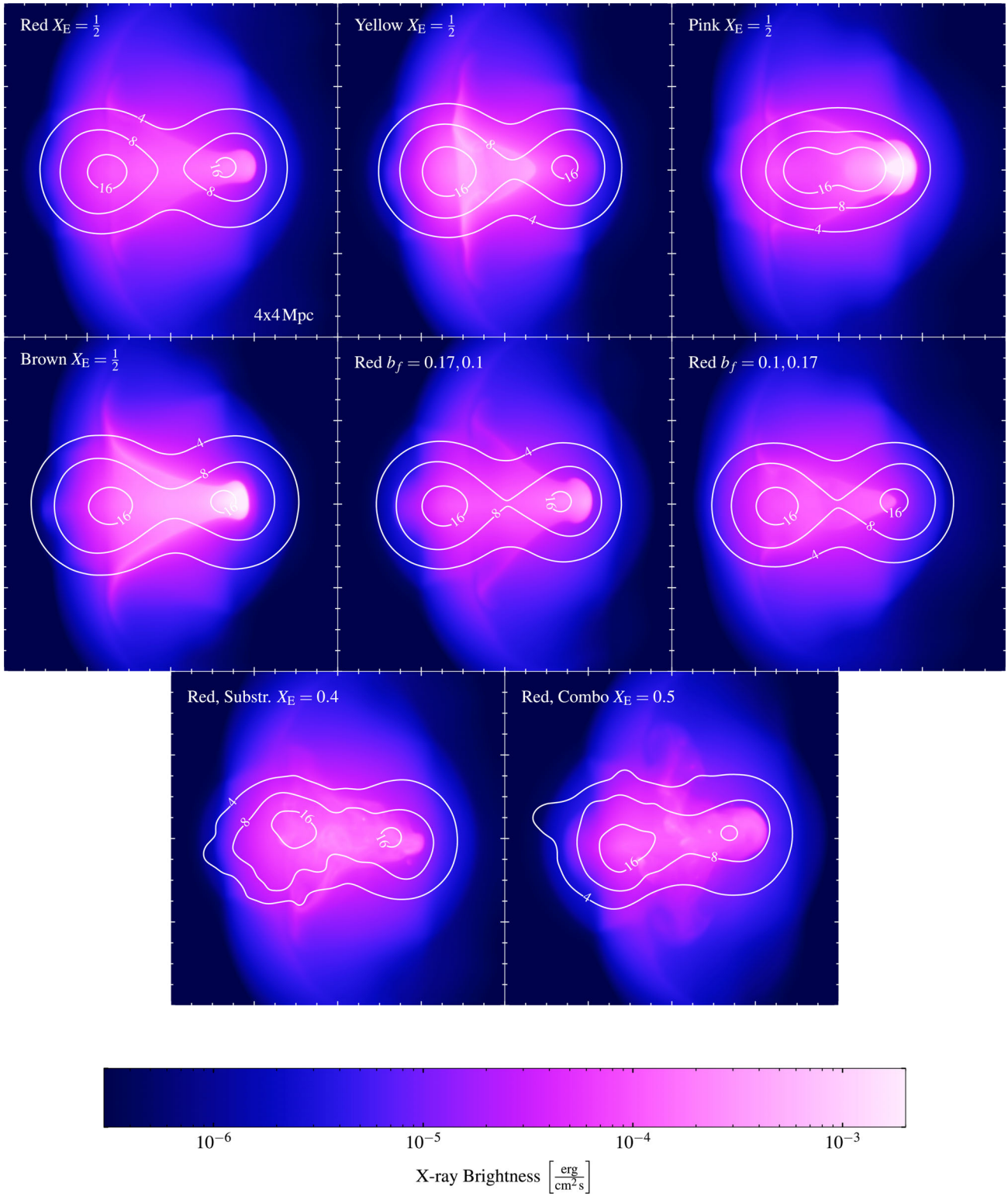

Figure 9. Projected X-ray emissivity of eight models with initial velocity: standard Red, Yellow, Pink, Brown and Red with reduced baryon fraction, including substructure and including both. We overplot contours of the DM mass distribution in 10^{21} g cm^{-2}.

At a shock distance of 3 Mpc, the observed state, both systems have $M_{500} \approx 1.5\,\mathrm{M}_\odot$ and $R_{500} \approx 1650$ kpc, and $M_{200} \approx 2.1\,\mathrm{M}_\odot$ and $R_{200} \approx 2500$ kpc, well in line with the weak lensing observations.

We show X-ray and temperature projection in Figs 9 and 10, panels 7 and 8. The X-rays show an elongated disturbed morphology similar to the observed cluster, where the cool core of the northern progenitor is ablated in the ICM of the southern progenitor. The DM core distance is roughly 1 Mpc. In the temperature map, we find two well-defined shocks. The NS is 1 Mpc (2 Mpc) in size for the standard (reduced) baryon fraction model. Temperatures reach up

Downloaded from https://academic.oup.com/mnras/article-abstract/471/4/4587/4002678 by guest on 20 November 2018

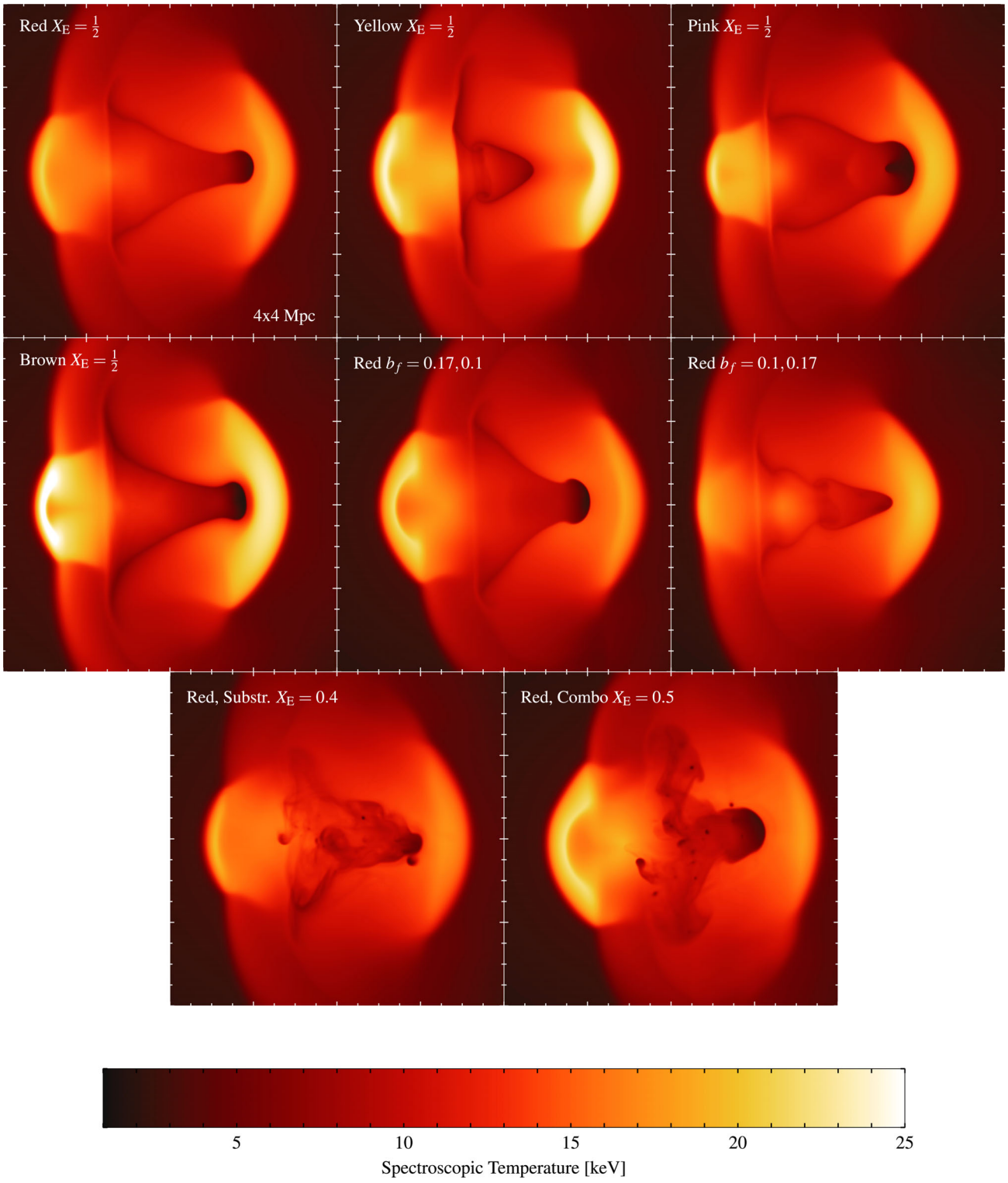

Figure 10. Projected Spectroscopic temperature of eight models with initial velocity: standard Red, Yellow, Pink, Brown and Red with reduced baryon fraction, including substructure (Red, Substr.) and including both (Red, Combo).

to 25 keV in a narrow region behind the shock. The SS is larger in the standard Red model and smaller in the reduced baryon fraction model.

In Fig. 13, we show Mach number histograms of the system at merger state. We find that the NS has a peak Mach number of 4.5, the SS of 3.2 in both models. We show shock speed distributions in Fig. 14 for both models. Velocity distributions are peaked around 4100 km s^{-1} (NS) and 3300 km s^{-1} (SS). We conclude that the model with reduced baryon fraction in the southern progenitor is most consistent with the high Mach number scenario and the majority of observations.

Downloaded from https://academic.oup.com/mnras/article-abstract/471/4/4587/4002678 by guest on 20 November 2018

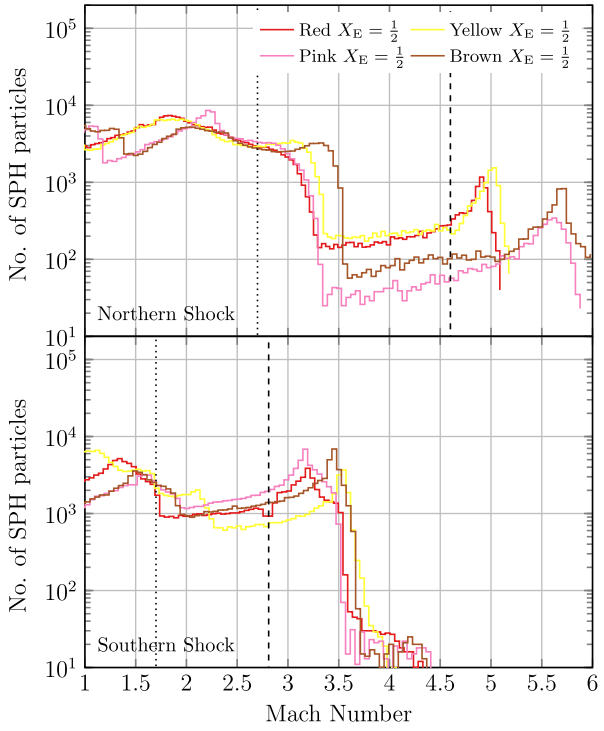

Figure 11. Binned Mach number distribution in the NS (top) and SS (bottom) from our Mach finder for the Black model with $X_E = 0$ and $X_E = 0.5$.

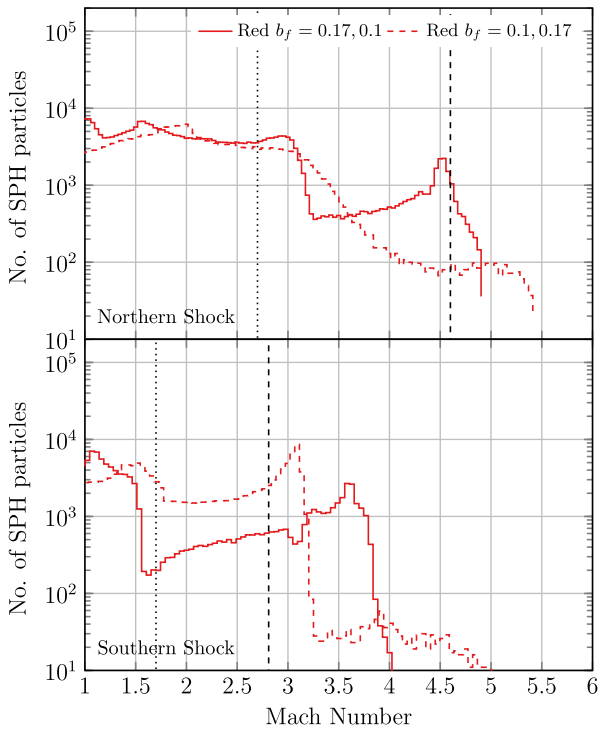

Figure 12. Binned Mach number distribution in the NS (top) and SS (bottom) from our Mach finder for the Red model with $b_{f,0} > b_{f,1}$ (solid) and $b_{f,0} < b_{f,1}$ (dashed).

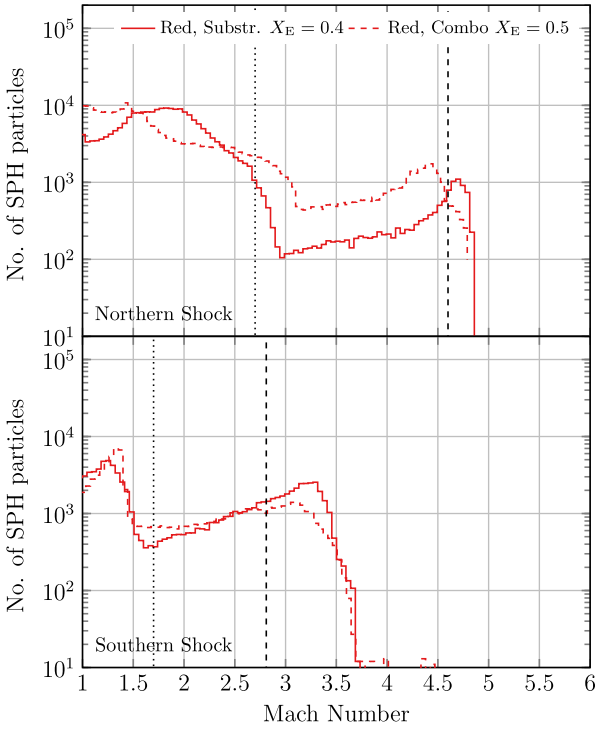

Figure 13. Binned Mach number distribution in the NS (top) and SS (bottom) from our Mach finder for the Red model with substructure.

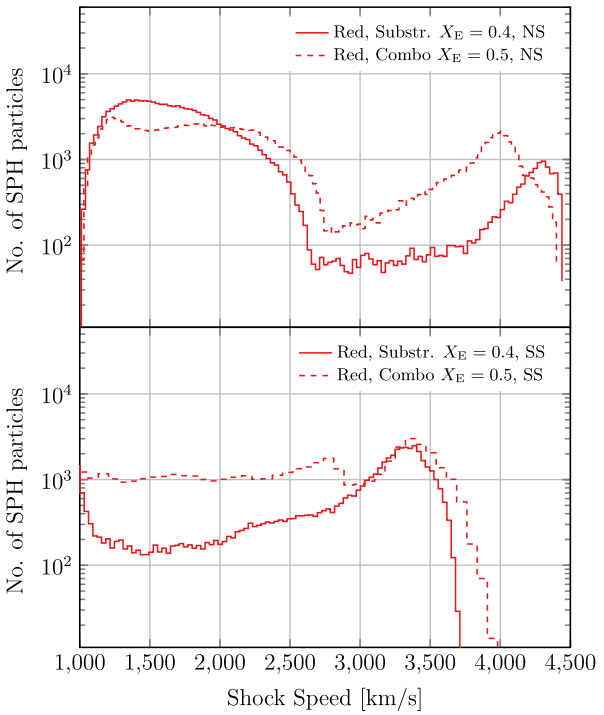

Figure 14. Binned shock velocity distribution in the NS (red, solid) and SS (red, dashed).

Downloaded from https://academic.oup.com/mnras/article-abstract/471/4/4587/4002678 by guest on 20 November 2018

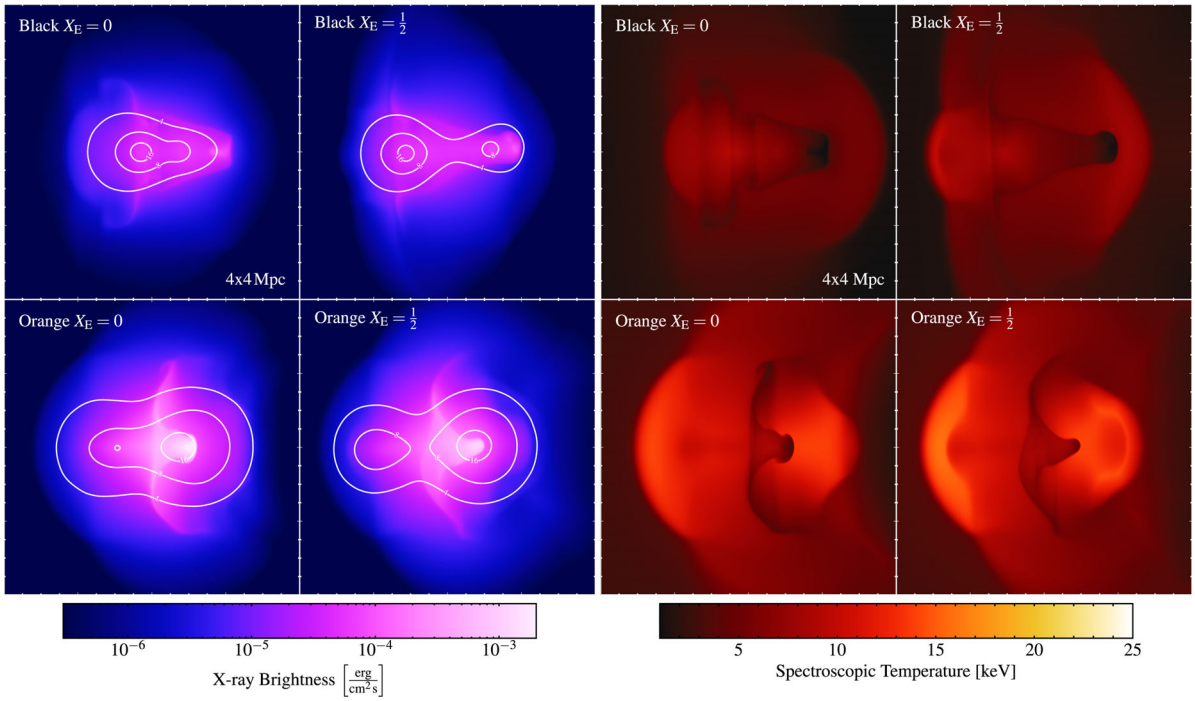

Figure 15. Left: projected X-ray emissivity in erg cm^{-2} Hz^{-1} s^{-1} of models Black and Orange, with and without initial velocity. We overplot contours of the DM mass distribution in 10^{21} g cm^{-2}. Right: spectroscopic temperature of the same models.

5.6 Models for the low Mach number scenario

In this section, we explore two model classes further outside the observed parameter range to force slower speeds in the NS : A model with a mass ratio smaller than 1 (Orange) and a model with large cut-off radius (Black). Both lead to a reduced Mach number in the NS. The Black mode allows a lower total mass and thus lower potential energy in the system. The Orange model decreases the mass of the progenitor driving the NS, at the cost of obtaining a higher Mach number in the SS.

We again show X-ray and temperature projections in Fig. 15 and Mach number distribution in Fig. 16. Basic model parameters can be found in Tables 1 and 2.

5.6.1 A model with $R_{cut} \gg r_{200}$

To test the limits of what is allowed with our cluster model, we simulate a model with a very large value for $R_{cut} \to \infty$ (Black model, Fig. 15, top row). The Black model with large cut-off radius shows structural properties similar to the Red model, however, at a lower X-ray luminosity ($L_X \approx 2 \times 10^{44}$ erg cm^{-2} s^{-1} Hz^{-1}). We find a triangular shape in the X-rays with a core distance of 500 kpc in the slow and 1 Mpc in the fast variant. ICM temperatures range from 10 to 20 keV, with the NS again standing out with 25 keV and the SS with 20 keV. Even though shock velocities are lower compared to the Red model, 3000 (NS) and Mach numbers in the faster variant of 5 (NS) and 2.7 (SS) are surprisingly consistent with the high Mach number scenario, not the low Mach number scenario. Shock speeds are slower than in the high Mach number scenario though, 3200 km s^{-1} (NS) and 2040 km s^{-1} (SS), as expected from a low-mass model. We conclude that the Black model is not a good fit to either of the scenarios. In our cluster model, lower mass systems cannot be consistent with the X-ray temperature upstream of the shocks.

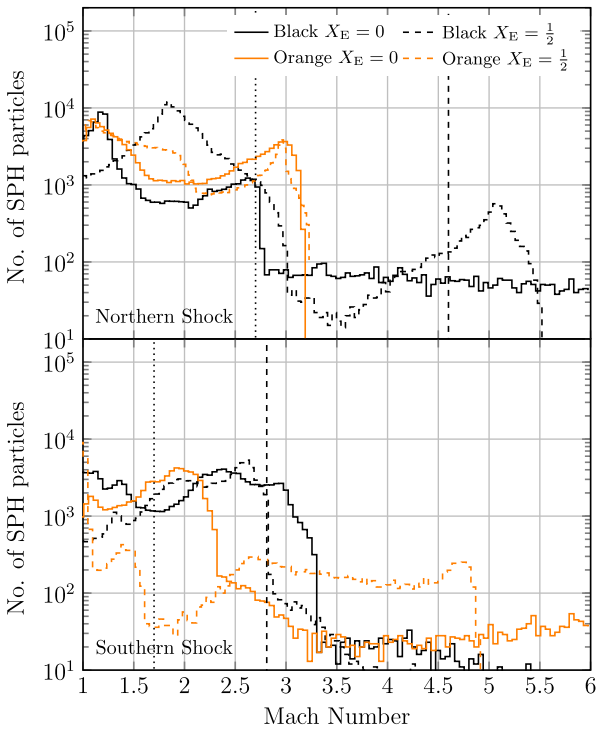

Figure 16. Binned Mach number distribution in the NS (top) and SS (bottom) from our Mach finder for the Orange and Black model with $X_E = 0$ (solid) and $X_E = 0.5$ (dashed).

5.6.2 A model with $X_M < 1$

Finally, we simulate a model with inverted mass ratio $X_M = \frac{1}{2}$ (Orange). We find a concentrated X-ray morphology with two

Downloaded from https://academic.oup.com/mnras/article-abstract/471/4/4587/4002678 by guest on 20 November 2018

Table 2. Model name, baryon fraction, X-ray luminosity at observed state in 10^{44} erg s^{-1}, initial merger velocities in km s^{-1}, Mach number of NS and SS in km s^{-1}, shock speeds of NS and SS for numerical models with $X_E = \frac{1}{2}$.

Name	$b_{f,0}$	$b_{f,1}$	L_x	$v_{0,0}$	$v_{0,1}$	M_{NS}	M_{SS}	v_{NS}	v_{SS}	t_{travel}
Red	0.17	0.17	6.3	664	−521	4.8	3.3	4367	3324	625
Yellow	0.17	0.17	11	746	−548	4.9	3.5	4647	3951	500
Brown	0.17	0.17	16	628	−534	5.5	3.3	5150	3352	575
Pink	0.17	0.17	14	710	−558	5.6	3.4	5262	3774	500
Red, sub	0.17	0.17	7	531	−333	4.6	3.3	4221	3399	675
Red, combo	0.17	0.1	5.2	664	−521	4.4	3.4	4081	3251	575
Black	0.17	0.17	2	565	−395	3.0	4.6	2253	3259	600
Orange	0.17	0.17	7.8	338	−507	5.1	2.7	3165	2040	775

characteristic contact discontinuities in the centre of the system (Fig. 15, bottom four panels). DM peak separation in the slow and the fast variant for the model is 1 Mpc. Temperatures in the centre of the cluster are roughly 10 keV, but reach again 25 keV in both shocks. The NS is larger than 2 Mpc in both variants, while the SS has an elongated size of only 1 Mpc. Mach numbers in the NS are roughly 3 in both variants. However, in the SS we find a Mach number of 2.2 in the slow model and 4.6 in the fast model. This is confirmed by the Mach number distributions (Fig. 16). We note that the SS in the slow model is not fully developed and shows a long tail of particles with high Mach numbers of up to 6. A model with inverted mass ratio is consistent with some aspects of the low Mach number scenario (Mach number in the NS, shock speeds in both shocks), but is inconsistent with other properties (shock temperature, shock morphology, SS properties). Hence, we conclude that none of our models are an acceptable fit to the low Mach number scenario of the two shocks.

6 DISCUSSION

6.1 The high Mach number scenario

Using our simulations we have found a class of models which is widely consistent with the high Mach number scenario. Assuming a cut-off radius consistent with observations of the Perseus cluster, simulations with a combined progenitor mass of $M_{tot} = 1.5$–2×10^{15} M$_\odot$, and a mass ratio of $X_M = 1.5$–2.5 generate shocks consistent with the observed radio relics (models Red, Yellow, Brown, Pink). Lower combined progenitor masses require larger cut-off radii (r_{cut}) to match the upstream shock properties, with lowest masses of around 0.75×10^{15} M$_\odot$ (model Black).

The X-ray brightness suggests a combined progenitor mass around $M_{tot} = 1.5 \times 10^{15}$ M$_\odot$, mostly dependent on the slope of the beta profiles (compare models Red and Pink) and the assumed Baryon fraction. As noticed before (Hoang et al. 2017), the system is underluminous with respect to the standard L_x–M relation, which is consistent with our best-fitting model that has very flat ICM density profiles and where the southern progenitor has a low Baryon fraction in the ICM (Hoang et al. 2017).

In simulations consistent with the high Mach number scenario, the shock that forms the northern relic travels outward along the merger axis. It is collimated by the contact discontinuities formed between the merging two ICM's. In the fiducial parameter region, shock speeds in the simulations lie around 4000 km s^{-1}, Mach numbers between 4 and 5. This is true over a wide range of masses, compare Mach numbers from Black and Red with $X_E = 0.5$. This is because lower merger masses result in lower shock speeds, but also lower upstream sound speeds. Thus, the Mach number in the shocks is only weakly dependent on mass.

Temperatures in the NS reach 20–25 keV in a <200 kpc region behind the shock, as expected from an upstream temperature of 3 keV and a Mach number above 4. We note that our simulations could well be resolution limited here, i.e. the true high temperature region is likely even smaller. We defer a resolution study to future work. The simulated SS shows a lower Mach number of 3–3.5, with speeds of about 3200 km s^{-1} and again temperatures of 15–20 keV, also roughly consistent with the high Mach number scenario. Our approach is not able to model the complex bulk flows, shock structure and galaxy shock interaction taking place in the SR. In particular, emission from radio galaxies in the SR can steepen the spectral index of the relic and decrease the Mach number inferred from the radio spectrum of the SR. We note that the large size of the SS in the simulations (2 Mpc) is indeed roughly consistent with new low-resolution LOFAR data of the SR (Hoang et al. 2017).

The main discrepancy of our simulations with the observed high Mach number scenario is the exact timing of the merger state, i.e. the NS tends to be too small when both shocks have a distance of 3 Mpc. We were able to show that different relative Baryon fraction could account for this (compare the two substructure models). The small β parameter and the X-ray brightness also suggest that the southern progenitor likely has a lower Baryon fraction than simulated, so the mass of the southern halo is likely larger than in our fiducial model. We set to the canonical cosmological value inside r_{200} of $b_f = 17$ per cent $\approx \frac{\Omega_b}{\Omega_{DM}}$ (e.g. Vikhlinin et al. 2006; Gonzalez et al. 2013; Planck Collaboration XVI 2014). However, this parameter varies significantly among observed clusters, depending on how much of the ICM has been converted into stars in galaxies since the last major merger [Perseus: $b_f = 23$ per cent (Simionescu et al. 2011), Cygnus: $b_f \leq 10$ per cent (Halbesma et al., in preparation)].

Given the number of parameters and their error bars we do not attempt to refine our models even further. We have likely reached the limit of what a toy model can achieve in reproducing a complex merging cluster.

6.2 The low Mach number scenario

We were not able to model the low Mach number scenario using our simulations in a satisfactory way. None the less, low-mass models generally reproduce some aspects of the low Mach number scenario. The Black model without initial velocity shows a Mach number of 2.6 and a shock velocity around 2000 km s^{-1} in the NS. However, the SS is too fast with Mach numbers of about 3 and velocities of

Downloaded from https://academic.oup.com/mnras/article-abstract/471/4/4587/4002678 by guest on 20 November 2018

2000 km s^{-1}, when 1.7 (!) is inferred from the X-ray observations. Giving the merger an initial velocity results in an NS consistent with the high Mach number scenario, the model is 'unstable' under this assumption.

The Orange model without initial velocity does a little better, with Mach numbers of about 3 in the NS and about 2 in the SS. Again, these values change drastically once the clusters are set on a non-zero orbit. Furthermore, the small SS in the simulation is inconsistent with recent observations of the cluster with LOFAR (Hoang et al. 2017).

Leaving this aside, it seems that we would need to reduce the total mass of the system even further, to allow for an initial velocity to fit the low Mach number scenario (less than model Blue). However, Black and Orange models are already very underluminous in the X-rays. Steeper β profiles for the ICM would increase the X-ray luminosity of a low-mass system, but decrease the upstream temperatures and thus increase the Mach number. This makes it not possible for us to fit X-ray luminosity and upstream temperature simultaneously. This circular argument suggests that the low Mach number scenario becomes inconsistent with itself at low masses.

All simulations show temperatures too high to be consistent with the low Mach number scenario behind the shocks. In shocks with consistent Mach numbers (Orange and Black), this points to an excess in upstream temperature or shock velocity. Our simulations assume the ICM behaves like a single fluid in the shocked region, which might very well be incorrect. One solution for the Mach number inconsistency could be a two-temperature structure of the ICM behind the shock. Here the thermal electrons, which are visible in the X-rays would have a temperature different from the thermal ions that mediate the shock. This has been observed on galaxy scales in the centre of clusters (Gu et al. 2012), but not been detected in shocks in the outskirts (Markevitch 2006; Russell et al. 2012).

We note that the fluid assumption for the ICM, as derived from Coulomb collisions in the *Spitzer* model (Spitzer 1956; Sarazin 1988) is indeed not valid in the region of the Sausage relic. Given the physical shock properties assumed here, Coulomb mean free paths of thermal ions in the NS are about $d_{\rm mfp,C} \approx 200$ kpc ahead of the relic. We would then expect a shock thickness of at least of that order. However, the *relic* thickness at 610 MHz is observed around 50 kpc. As the relic emission is caused by cooling cosmic ray electrons, the injection region has to be at least an order of magnitude smaller than its extent to result in the observed steepening of the spectral index profile. Thus, another process has to maintain collisionality of thermal protons and cosmic rays in the shock and ahead of the relic. It is unclear why the thermal electrons should not be heated, but cosmic ray electrons seem to be efficiently injected or re-accelerated.

Alternatively, if collisionality in the ICM is maintained through the interaction of particles with plasma waves, the fluid approximations is valid far below kpc scale (e.g. Brunetti & Jones 2014; Donnert & Brunetti 2014, and references therein). In this case, we would expect high temperatures for the thermal electrons behind the shock as well and other effects are responsible for the inconsistency in Mach number. If indeed radio haloes are caused by turbulent re-acceleration (Petrosian 2001), they are direct evidence for this mechanism acting on radio dark cosmic ray electrons.

6.3 Merger speed versus shock speed

Shock speeds in the high Mach number scenario are only reproduced for orbits with a zero energy fraction of $X_{\rm E} \geq 0.4$ (compare Red with and without initial velocities). This is not surprising given that clusters likely detach from the Hubble flow before their virial radii touch. Following Sarazin (2002), the combined in-fall velocity v_0 of the progenitors at a distance d with impact parameter b_0 before the merger is connected to the distance d_0 at which both progenitors began to merge:

$$v_0 \approx 2930 \sqrt{\frac{M_0 + M_1}{10^{15}\,{\rm M}_\odot}} \left(\frac{d}{1\,{\rm Mpc}}\right)^{-(1/2)} \left[\frac{1 - \frac{d}{d_0}}{1 - \frac{b_0^2}{d_0^2}}\right]^{1/2} \quad {\rm km\ s^{-1}}. \quad (8)$$

For the fiducial model with substructure (Red), we then find an initial separation of 4500 Mpc, 30 per cent larger than the combined virial radius of the progenitors.

We can compare the speeds of the merger with the shock speeds in the two scenarios: we plot the in-fall velocity v_0 at a distance of combined virial radii (dotted) and half that value (solid, about 2 Mpc) in Fig. 17 for a mass range of 0.1–2.5 $\times$ 10^{15} M$_\odot$. We add the fiducial model as red circle, the velocity is independent of mass ratio. We overplot the shock velocity in the low Mach number scenario as black dashed line.

In-fall velocities are only a fraction of the shock speed in the high Mach number scenario (4200 km s^{-1}) for all relevant mass ranges, even at a distance of half the combined virial radii. This is consistent with the simulations, where a large fraction of the shock kinetic energy is generated during core passage, when the DM cores rapidly interact and drive two shocks outwards.

In contrast, the shock speed of the low Mach number scenario, 2100 km s^{-1}, is exceeded at cluster in-fall for all combined masses larger than 10^{15} M$_\odot$ at a distance of half the virial radius (2–3 Mpc). Any additional kinetic energy by e.g. DM core interaction will lead to shock velocities too high to be consistent with the low Mach number scenario. This kinetic argument motivates why we would need very small cluster masses ($M_0 + M_1 \approx 10^{14}$ M$_\odot$) to reproduce the shock speeds in the low Mach number scenario. Cluster in-fall speeds alone are inconsistent with the shock speeds estimated in the low Mach number scenario for systems consistent with weak lensing observations.

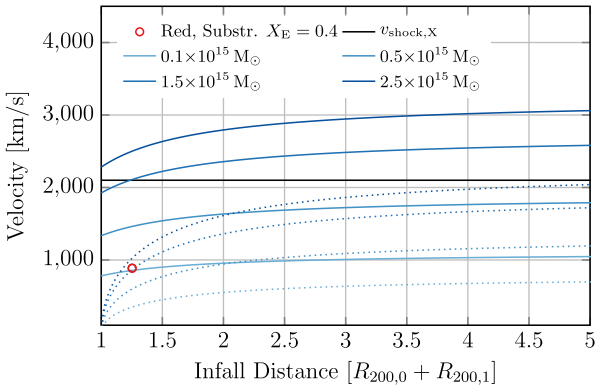

Figure 17. Combined in-fall velocity at the distance of the two virial radii in km s^{-1} over merger distance in units of that distance.

6.4 Cluster masses versus merger state

In our approach, clusters scale with combined progenitor mass, so morphological properties remain widely identical over a mass range, holding $X_{\rm E}$, $b_{\rm f}$, β and the mass ratio constant (compare Red and Black). However, the dynamical state of the system at observation time changes with cluster mass, because the characteristic velocities

Downloaded from https://academic.oup.com/mnras/article-abstract/471/4/4587/4002678 by guest on 20 November 2018

(equation 8) and length-scales of the system (r_{200}) change. However, the observed shock distance remains the same (3 Mpc). The most notable effect is that the distance of the DM mass peaks decreases with decreasing cluster mass (keeping X_E constant). The second core passage is occurring at the observed state for masses of about 10^{14} $M_\odot$ (if the system is started at rest, see model Black with $X_E = 0$).

In the slow low-mass simulations, this results in a core distance significantly smaller than observed (Black, Purple). In these models, the DM cores have turned around and are shortly before second core passage, when the shocks are at 3 Mpc distance. This sets a lower limit on the total mass of the system, which is roughly 10^{15} $M_\odot$ for $X_E = 0$. The slowest allowed model (Green) still predicts shock velocities inconsistent with the low Mach number scenario. This suggests that the low Mach number scenario is not consistent with the merger state of the observed system, as inferred from the weak lensing mass peaks.

6.5 Guiding future observations

Our results strongly suggest to use X-ray observatories to search for excess temperatures in the downstream region of the NS of CIZA J2242.8+5301 and shocks in other cluster with a radio-derived Mach number larger than 4. We note that the shock surface is not yet been detected with *Chandra*, the only X-ray instrument with comparable resolution to LOFAR. Thus, the estimate of the Mach number from the surface brightness jump cannot be considered very robust. A detection would also allow us to examine spatial co-location of shock and relic. If the size of the shock surface exceeds the size of the relic, this would imply fluctuation in Mach number or upstream CR electron density.

Our numerical models, combined with current observations, including the total X-ray brightness from *ROSAT*, clearly favour the high Mach number scenario, with $M > 1.5 \times 10^{15}$ $M_\odot$, Mach numbers above 4 and shock velocities above 1000 km s^{-1}. Among the simulations, post-shock temperatures regularly exceed 15 keV, however, in a small area on the sky with very low X-ray emissivity. Thus, a long exposure with the optimal instrument might be necessary to find a high-temperature component and clearly detect the shock front. We plan to use our fiducial model with simulators for X-ray observatories (Marx, SIXTE etc.) to find the optimal instrument and exposure parameters for this search in a future paper.

Another clue to the total mass of the system could come from the SZ effect of the total cluster. The SZ-mass scaling relation is reasonably tight to confirm the weak lensing mass measurements and support or weaken the high Mach number scenario. We are currently not aware of a successful measurement of the Compton-Y parameter in CIZA J2242.8+5301 (Stroe et al. 2014b; Basu et al. 2016). We show a prediction of the projected Compton-Y parameter from the fiducial model in Fig. 18. We overplot the X-ray emission in white contours in units of 10^{-6} erg s^{-1} cm^{-2}.

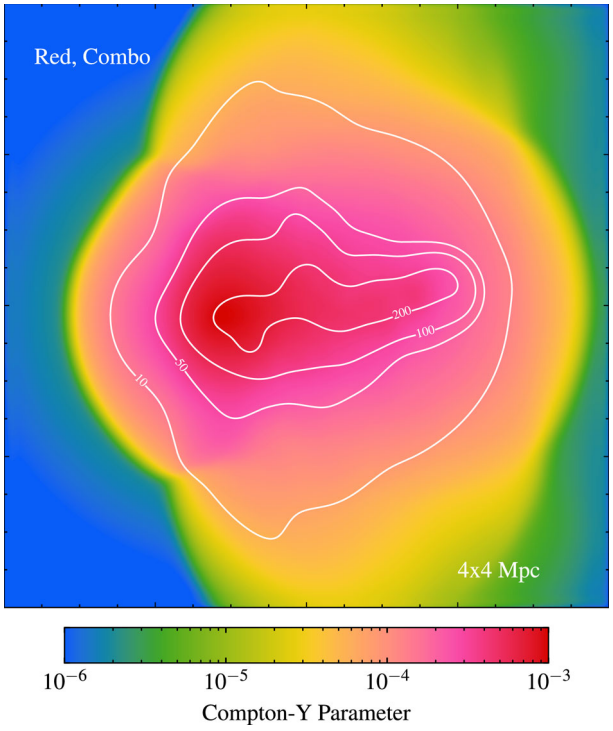

Figure 18. Projected Compton-Y parameter from the Red model with substructure and reduced Baryon fraction. In contours X-ray brightness in 10^{-6} erg s^{-1} cm^{-2} in the *ROSAT* band.

7 CONCLUSIONS

We attempted to find a model for the merging galaxy cluster CIZA J2242.8+5301 and its two prominent shocks. We showed analytically that in the NS, upstream X-ray temperatures and radio properties are consistent with each other. These values are in turn consistent with weak lensing cluster masses, assuming a reasonable model for the underlying merger progenitors. We then explored the resulting parameter space using idealized simulations of galaxy cluster mergers, where we modelled the northern progenitor as a cool core. We found that models with a combined progenitor mass of $M_{\rm tot,200} = 1.5$–2×10^{15} $M_\odot$ and mass ratios between 1.5 and 2.5 are consistent with the majority of observations. In particular:

(i) X-ray brightness, morphology and upstream shock temperature;
(ii) weak lensing total mass, subcluster mass ratio and location of the mass peaks;
(iii) size of the shocks, their radio inferred Mach numbers and shock speeds.

We were not able to find a model that is consistent with all the X-ray observations, in particular the observed downstream temperatures. Even the most conservative models for the cluster dynamics show shock speeds and thus downstream temperatures larger than observed. In particular:

(i) kinetic arguments suggest that X-ray-derived shock speeds cannot be reproduced for models with masses above 0.5×10^{15} $M_\odot$;
(ii) models with masses below 0.5×10^{15} $M_\odot$ are underluminous in the X-rays;
(iii) the observed DM core distance is inconsistent with simulations that reproduce X-ray-derived shock speeds.

We concluded that the high Mach number scenario is preferred by the observations and simulations. An extensive search for a high-temperature component and surface brightness jump at the NS using X-ray observatories should be able to clarify the situation and support or rule out the low Mach number scenario.

ACKNOWLEDGEMENTS

We thank the anonymous referee for helpful comments that significantly improved the manuscript. The authors also thank Aurora

Downloaded from https://academic.oup.com/mnras/article-abstract/471/4/4587/4002678 by guest on 20 November 2018

Simionescu, Irina Zhuravleva and Ondrej Urban for providing the observed profiles of the Perseus cluster. JD thanks Carlo Giocoli for extensive discussions about DM substructure in clusters. We thank Tom Jones for discussions and access to the Itasca cluster at MSI for this research. The research leading to these results has received funding from the People Programme (Marie Sklodowska Curie Actions) of the European Unions Eighth Framework Programme H2020 under REA grant agreement no 658912, 'Cosmo Plasmas'. HR acknowledges support from the European Research Council Advanced Investigator programme NewClusters 321271. We used Julia[3] and PGFPlots for all graphics in this document. All colour maps are perceptually uniform (Kovesi 2015, colorbrewer.org).

REFERENCES

Akamatsu H., Kawahara H., 2013, PASJ, 65, 16
Akamatsu H. et al., 2015, A&A, 582, A87
Barnes J. E., 2012, MNRAS, 425, 1104
Bartelmann M., Steinmetz M., 1996, MNRAS, 283, 431
Basu K., Vazza F., Erler J., Sommer M., 2016, A&A, 591, A142
Beck A. et al., 2016a, MNRAS, 455, 2110
Beck A., Dolag K., Donnert J., 2016b, MNRAS, 458, 2080
Binney J., Tremaine S., 2008, Galactic Dynamics, 2nd edn. Princeton Univ. Press, Princeton, NJ
Botteon A., Gastaldello F., Brunetti G., Kale R., 2016, MNRAS, 463, 1534
Brüggen M., Bykov A., Ryu D., Röttgering H., 2012, Space Sci. Rev., 166, 187
Brunetti G., Jones T. W., 2014, Int. J. Mod. Phys. D, 23, 30007
Brunetti G., Rudnick L., Cassano R., Mazzotta P., Donnert J., Dolag K., 2013, A&A, 558, A52
Burns J. O., Loken C., Roettiger K., Norman M. L., Clarke D. A., 1993, in Röser H.-J., Meisenheimer K., eds, Lecture Notes in Physics, Vol. 421, Jets in Extragalactic Radio Sources. Springer-Verlag, Berlin, p. 267
Cavaliere A., Fusco-Femiano R., 1976, A&A, 49, 137
Corless V. L., King L. J., 2007, MNRAS, 380, 149
Dawson W. A. et al., 2015, ApJ, 805, 143
Diehl S., Rockefeller G., Fryer C. L., Riethmiller D., Statler T. S., 2012, preprint (arXiv:e-prints)
Dolag K., Stasyszyn F., 2009, MNRAS, 398, 1678
Donnert J. M. F., 2014, MNRAS, 438, 1971 (D14)
Donnert J., Brunetti G., 2014, MNRAS, 443, 3564
Donnert J. M. F., Stroe A., Brunetti G., Hoang D., Roettgering H., 2016, MNRAS, 462, 2014
Duffy A. R., Schaye J., Kay S. T., Dalla Vecchia C., 2008, MNRAS, 390, L64
Eddington A. S., 1916, MNRAS, 76, 572
Feretti L., Giovannini G., Govoni F., Murgia M., 2012, A&AR, 20, 54
Gao L., De Lucia G., White S. D. M., Jenkins A., 2004, MNRAS, 352, L1
Giocoli C., Bartelmann M., Sheth R. K., Cacciato M., 2010, MNRAS, 408, 300
Gonzalez A. H., Sivanandam S., Zabludoff A. I., Zaritsky D., 2013, ApJ, 778, 14
Govoni F., Feretti L., 2004, Int. J. Mod. Phys. D, 13, 1549
GSL Project C., 2010, GSL - GNU Scientific Library - GNU Project - Free Software Foundation (FSF), Available at: http://www.gnu.org/software/gsl/
Gu L. et al., 2012, ApJ, 749, 186
Harwood J. J., Hardcastle M. J., Croston J. H., Goodger J. L., 2013, MNRAS, 435, 3353
Hernquist L., 1990, ApJ, 356, 359
Hoang D. et al., 2017, MNRAS, submitted
Hoeft M., Brüggen M., Yepes G., Gottlöber S., Schwope A., 2008, MNRAS, 391, 1511
Hong S. E., Ryu D., Kang H., Cen R., 2014, ApJ, 785, 133
Hong S. E., Kang H., Ryu D., 2015, ApJ, 812, 49
Iapichino L., Brüggen M., 2012, MNRAS, 423, 2781
Jee M. J. et al., 2015, ApJ, 802, 46
Kang H., Ryu D., 2015, ApJ, 809, 186
Kang H., Ryu D., 2016, ApJ, 823, 13
Kang H., Ryu D., Jones T. W., 2017, ApJ, 840, 42
Kazantzidis S., Magorrian J., Moore B., 2004, ApJ, 601, 37
Kocevski D. D., Ebeling H., Mullis C. R., Tully R. B., 2007, ApJ, 662, 224
Kovesi P., 2015, preprint (arXiv:e-prints)
Kravtsov A. V., Borgani S., 2012, ARA&A, 50, 353
Lage C., Farrar G., 2014, ApJ, 787, 144
Markevitch M., 2006, in Wilson A., ed., ESA SP-604: The X-ray Universe 2005. ESA, Noordwijk, p. 723
Markevitch M., Vikhlinin A., 2007, Phys. Rep., 443, 1
Mazzotta P., Rasia E., Moscardini L., Tormen G., 2004, MNRAS, 354, 10
Miniati F., Ryu D., Kang H., Jones T. W., Cen R., Ostriker J. P., 2000, ApJ, 542, 608
Molnar S. M., Broadhurst T., 2017, ApJ, 841, 46
Navarro J. F., Frenk C. S., White S. D. M., 1996, ApJ, 462, 563
Ogrean G. A., Brüggen M., Röttgering H., Simionescu A., Croston J. H., van Weeren R., Hoeft M., 2013, MNRAS, 429, 2617
Ogrean G. A., Brüggen M., van Weeren R., Röttgering H., Simionescu A., Hoeft M., Croston J. H., 2014, MNRAS, 440, 3416
Okabe N., Akamatsu H., Kakuwa J., Fujita Y., Zhang Y., Tanaka M., Umetsu K., 2015, PASJ, 67, 114
Petrosian V., 2001, ApJ, 557, 560
Pfrommer C., Springel V., Enßlin T. A., Jubelgas M., 2006, MNRAS, 367, 113
Planck Collaboration XVI, 2014, A&A, 571, A16
Press W. H., Teukolsky S. A., Vetterling W. T., Flannery B. P., 1992, Numerical recipes in FORTRAN. The art of scientific computing. Cambridge Univ. Press, Cambridge
Roettiger K., Burns J. O., Stone J. M., 1999, ApJ, 518, 603
Russell H. R. et al., 2012, MNRAS, 423, 236
Sarazin C. L., 1988, X-ray Emission from Clusters of Galaxies. Cambridge Univ. Press, Cambridge
Sarazin C. L., 2002, in Feretti L., Gioia I. M., Giovannini G., eds, Astrophysics and Space Science Library, Vol. 272, Merging Processes in Galaxy Clusters. Kluwer, Dordrecht, p. 1
Schaal K. et al., 2016, MNRAS, 461, 4441
Schindler S., Mueller E., 1993, A&A, 272, 137
Shimwell T. W., Markevitch M., Brown S., Feretti L., Gaensler B. M., Johnston-Hollitt M., Lage C., Srinivasan R., 2015, MNRAS, 449, 1486
Simionescu A. et al., 2011, Science, 331, 1576
Skillman S. W., O'Shea B. W., Hallman E. J., Burns J. O., Norman M. L., 2008, ApJ, 689, 1063
Sobral D., Stroe A., Dawson W. A., Wittman D., Jee M. J., Röttgering H., van Weeren R. J., Brüggen M., 2015, MNRAS, 450, 630
Spitzer L., 1956, Physics of Fully Ionized Gases. Interscience Publishers, New York
Springel V., 2005, MNRAS, 364, 1105
Stroe A., van Weeren R. J., Intema H. T., Röttgering H. J. A., Brüggen M., Hoeft M., 2013, A&A, 555, A110
Stroe A., Sobral D., Röttgering H. J. A., van Weeren R. J., 2014a, MNRAS, 438, 1377
Stroe A. et al., 2014b, MNRAS, 441, L41
Stroe A., Harwood J. J., Hardcastle M. J., Röttgering H. J. A., 2014c, MNRAS, 445, 1213
Stroe A. et al., 2015, MNRAS, 450, 646
Stroe A. et al., 2016, MNRAS, 455, 2402
Tormen G., Diaferio A., Syer D., 1998, MNRAS, 299, 728
Urban O. et al., 2014, MNRAS, 437, 3939
van Weeren R. J., Röttgering H. J. A., Brüggen M., Hoeft M., 2010, Science, 330, 347
van Weeren R. J., Brüggen M., Röttgering H. J. A., Hoeft M., 2011, MNRAS, 418, 230
Vazza F., Brunetti G., Gheller C., 2009, MNRAS, 395, 1333

[3] www.julialang.org

Downloaded from https://academic.oup.com/mnras/article-abstract/471/4/4587/4002678 by guest on 20 November 2018

Vikhlinin A., Kravtsov A., Forman W., Jones C., Markevitch M., Murray S. S., Van Speybroeck L., 2006, ApJ, 640, 691
Zhuravleva I. et al., 2013, MNRAS, 435, 3111
ZuHone J. A., Kowalik K., 2016, preprint (arXiv:e-prints)

APPENDIX: A NON-COOL-CORE MODEL

We present a model with the same parameter configuration as the Red model (section 5.3), but as a non-cool-core merger, i.e. the northern progenitor has $r_{\rm core} = r_{\rm s}/3$. In Fig. A1, we show the X-ray (left) and the temperature projections (right) of the system at the observed state. The morphology of the system in the X-ray emission is not elongated and more diffuse than in the standard Red model, with a characteristic contact discontinuity in the centre of the cluster. The temperature structure in the shocks is similar to the standard Red model, but the characteristic elongated structure of the observed cluster is not present. X-ray luminosity, Mach numbers and dynamical parameters are roughly the same as in the standard Red model. We conclude that a non-CC merger is not favoured by the observed X-ray morphology of the cluster.

We note that recent simulations shown by Molnar & Broadhurst (2017) reproduce the elongated X-ray morphology with a non-CC merger, however, with much higher merger velocities than presented here. The velocities would immediately rule out the low Mach number scenario and are thus not in the scope of this work.

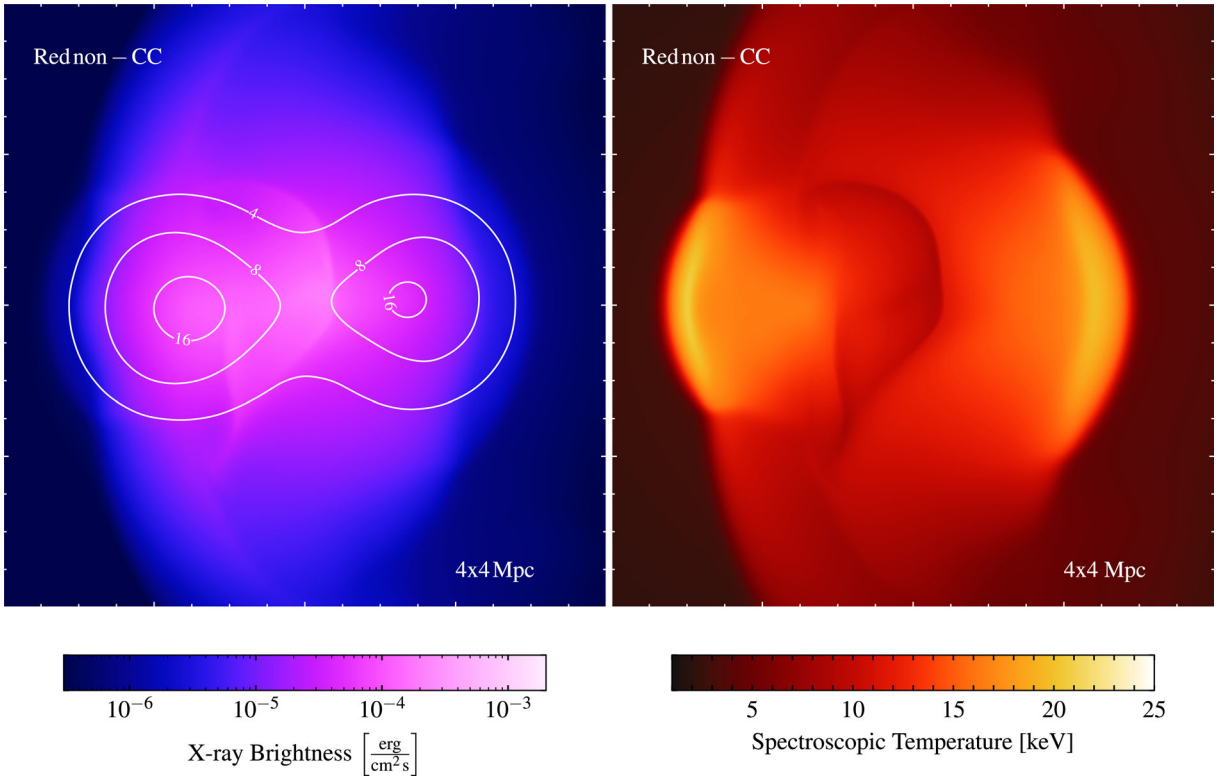

Figure A1. Left: projected X-ray emissivity in erg cm^{-2} Hz^{-1} s^{-1} of model Red without initial velocity, but without a cool core. We overplot contours of the DM mass distribution in 10^{21} g cm^{-2}. Right: spectroscopic temperature of the same models.

This paper has been typeset from a TEX/LATEX file prepared by the author.

Downloaded from https://academic.oup.com/mnras/article-abstract/471/4/4587/4002678 by guest on 20 November 2018